Journal Pre-proof

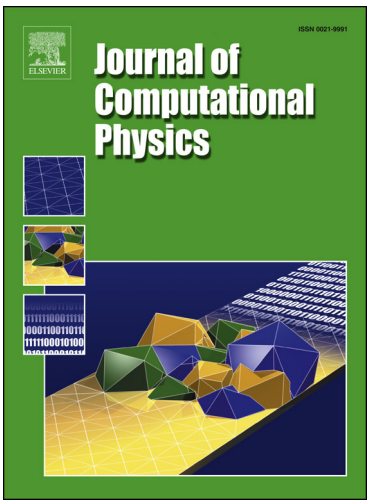

An immersed boundary-material point method for shock-structure interaction and dynamic fracture

Ruichen Ni, Jiasheng Li, Xiong Zhang, Xu Zhou and Xiaoxiao Cui

PII: S0021-9991(22)00620-9
DOI: https://doi.org/10.1016/j.jcp.2022.111558
Reference: YJCPH 111558

To appear in: *Journal of Computational Physics*

Received date: 19 November 2021
Revised date: 25 May 2022
Accepted date: 19 August 2022

Please cite this article as: R. Ni, J. Li, X. Zhang et al., An immersed boundary-material point method for shock-structure interaction and dynamic fracture, *Journal of Computational Physics*, 111558, doi: https://doi.org/10.1016/j.jcp.2022.111558.

Highlights

- IBM-MPM is proposed for simulations of FSI problems and dynamic fracture.
- lg-CFIB method is proposed by combining advantages of GCIB and penalty-IB method.
- lg-CFIBM satisfies the boundary velocity conditions strictly at each time step.
- lg-CFIBM has no need to reconstruct FSI interfaces when topology changes.

An immersed boundary-material point method for shock-structure interaction and dynamic fracture*

Ruichen Ni[a], Jiasheng Li[a], Xiong Zhang[a,*], Xu Zhou[b], Xiaoxiao Cui[b]

[a]School of Aerospace Engineering, Tsinghua University, Beijing 100084, PR China
[b]Beijing Special Engineering Design and Research Institute, Beijing 100028, PR China

Abstract

As a class of extreme fluid-structure interaction (FSI), shock-structure interaction problems are always accompanied with dynamic fracture phenomena in solid structure. During the dynamic fracture process, small fragments of thin geometry and fresh FSI interfaces will be generated, which makes the FSI interface difficult to be reconstructed. An immersed boundary-material point method (IBMPM) is proposed in this paper for simultaneous simulations of shock-structure interaction and accompanied dynamic fracture. The finite volume method (FVM) is employed as fluid solver and specifically a TVD Riemann solver is adopted for shock simulation, while the material point method (MPM) is employed as solid solver for simulation of extreme deformation problem. The FVM and MPM are then coupled by our improved immersed boundary method (IBM) which is named as Lagrangian continuous-forcing IBM (lg-CFIBM). The lg-CFIBM is proposed in the frame of continuous forcing approach with a compact support area for the immersed boundary conditions. It can guarantee the boundary velocity conditions strictly at each time step and has no need to reconstruct FSI interfaces. Several numerical examples, including shock-cylinder obstacle interaction, flexible panel deformation induced by shock wave and fragmentation driven by detonation, are studied to verify and validate the proposed method, and numerical results are in good agreement with experiments.

Keywords: shock-structure interaction, dynamic fracture, immersed boundary method, material point method, Riemann solver

1. Introduction

Shock-structure interaction is a class of extreme fluid-structure interaction (FSI) problems and always leads to dynamic fracture and fragmentation of solid structures in engineering applications, such as directed blasts, hyper velocity impact, sonic boom, and air explosion. For its importance in safety and security, shock-structure interaction problems with dynamic fracture have attracted extensive attention in recent decades. However, with the complex structure geometry and nonlinear material constitutive relation, the empirical conclusions obtained by specific experiments are not universal. Therefore, the development of efficient and powerful algorithms to simulate these phenomena is an active field of research.

Since being first introduced by Peskin[1] in 1970s, the immersed boundary method (IBM) has shown its success in simulating the interaction between fluid and structure with complex boundary geometry. The main feature of IBM is that fluid simulation is carried out on a Cartesian grid which does not conform to the structure geometry and additional procedure is applied to impose the effect of the immersed boundary on the flow. Therefore, various fully-developed methods could be chosen for CFD and CSD simulation individually. Mittal and Iaccarino[2] classified IBMs into continuous forcing approach and discrete forcing approach based on the way of applying FSI boundary conditions.

Continuous forcing approach adopts a feedback law to calculate the FSI force on the Lagrangian boundary points and then the force is smeared onto Eulerian fluid grid based on a smoothed approximation of the Dirac delta function[3–9]. This approach has a sound physical basis and is simple to implement, and thus is widely chosen by scholars for engineering simulations. Ye[10] coupled smoothed dissipative particle dynamics (SDPD) method and IBM of this approach to carry out the simulations of red blood cells in complex flow problems. Vasilakis[11]

*Supported by the National Natural Science Foundation of China (12172192).
*Corresponding author.
Email address: xzhang@tsinghua.edu.cn (Xiong Zhang)

employed this approach on cavitating flows with complex or moving boundaries. However, continuous forcing approach is implemented in a sense of penalty function method, and the slip or non-slip boundary conditions can not be satisfied strictly at each time step. Therefore, when simulating shock-structure interaction problems, shock structures sensitive to boundary velocity direction, such as Mach reflection, may vanish.

Discrete forcing approach imposes the boundary conditions on the immersed boundary, specifically with velocity conditions for fluid flow and force conditions for solid structure. Based on the way of applying boundary velocity conditions, this approach could be further classified into ghost cell approach [12–18] and cut cell approach [19–21]. This approach keeps track of a sharp interface between fluid and structure and satisfies boundary velocity conditions strictly at each time step, and thus is always used in shock-structure interaction simulations. Chaudhuri [22] adopted the ghost cell immersed boundary (GCIB) method to solve complex strong shock/obstacle interactions for both stationary and moving shock waves. Brehm [23] applied the immersed interface method (IIM) to the inflation of a supersonic parachute in the upper Martian atmosphere. However, this approach needs to calculate normal directions and vertical distances along the immersed boundary at each time step, which is time-consuming. Moreover, in the dynamic fracture simulations, small fragments of thin geometry and fresh FSI interfaces will be generated, which makes the FSI interface difficult to be reconstructed. To our best knowledge, there are few works on simultaneous simulations of shock-structure interaction and accompanied dynamic fracture.

Dynamic fracture simulations involve extreme structure deformation and nonlinear material constitutive relation. Traditional Lagrangian methods suffer from heavily distorted grid, and traditional Eulerian methods encounter the difficulty of recording historical variables. To avoid the above mentioned disadvantages of Lagrangian and Eulerian methods, Harlow [24,25] combined the concepts of Lagrangian and Eulerian method and proposed the particle-in-cell (PIC) method which discretizes the fluid into Lagrangian particles and computational domain into a uniform Eulerian mesh. Sulsky et al. extended the FLIP PIC methods [26,27] from fluid mechanics to solid mechanics and named this method as material point method (MPM) [28,29]. The MPM has shown its success in simulating extreme deformation events over two decades, such as hyper velocity impact [30–33], penetration [34,35], fracture evolution [36,37], fluid flow [38–40], fluid-structure interaction [41–43], and landslide [44,45]. Although MPM has been applied for fluid simulation in the literature, it suffers from numerical fracture and non-physical oscillation, especially in the gas simulation of high compressibility. Ma and Zhang [46] proposed adaptive particle splitting scheme of MPM to withstand numerical fracture phenomenon, which however is time-consuming and CPU-memory-consuming.

MPM and IBM have been coupled to simulate large deformation of solid structure in the FSI problems in a handful of literature. Gilmanov [17] combined hybrid immersed boundary method (HIBM) for handling complex moving boundaries and MPM for resolving structural stresses and movement. The HIBM and MPM approach provided excellent results in the simulations of incompressible fluid flow and large solid deformation. The topology of the FSI interface will heavily change in dynamic fracture which is the focus of the present work, while the exact position of the FSI interface is demanded in HIBM to calculate the boundary normal directions. And, the reconstruction of the fresh FSI interfaces form boundary particles in MPM is too difficult, unstable and time-consuming to be implemented, which still remains as an active research field called the surface reconstruction of 3-dimensional points cloud.

In the present work, the finite volume method (FVM) is employed as fluid solver and specifically a TVD Riemann solver is adopted for shock simulation, while the material point method (MPM) is employed as solid solver for simulation of extreme deformation problem. The FVM and MPM are then coupled by our improved immersed boundary method (IBM) which is named as Lagrangian continuous-forcing IBM (lg-CFIBM). The lg-CFIBM is proposed in the frame of continuous forcing approach with a compact support area for the immersed boundary conditions. It can guarantee the boundary velocity conditions strictly at each time step and has no need to calculate the normal directions and vertical distances along the immersed boundary anymore. Therefore, the lg-CFIBM is a promising method for simultaneous simulations of shock-structure interaction and accompanied dynamic fracture. The entire FSI numerical method is called as immersed boundary-material point method (IBMPM) in the rest of the paper. Several numerical examples, including shock-cylinder obstacle interaction, flexible panel deformation induced by shock wave and fragmentation driven by detonation, are studied to verify and validate the proposed method, and numerical results are in good agreement with experiments.

The rest of this paper is organized as follows. Governing equations of fluid and solid are briefly introduced in Section 2. Then MPM method for the solid structure, the discrete scheme for the Euler equations and the detailed procedure of lg-CFIBM are presented in Section 3, 4 and 5 respectively. Validations and benchmark simulations are presented in Section 6. Finally, conclusions and remarks are drawn in Section 7.

2. Governing equations

2.1. Updated Lagrangian formulation for solid structure

The finite element discretization with Lagrangian meshes can be classified into two categories, the updated Lagrangian approach and total Lagrangian approach. The stress and strain measures are defined with respect to the initial (reference) configuration in the total Lagrangian approach and the current configuration in the updated Lagrangian approach. The updated Lagrangian approach has been widely used in the MPM such that the governing equations are only given in the updated Lagrangian formulation here.

The conservation laws for mass, momentum and energy are given as

$$\dot{\rho} + \rho \nabla \cdot \dot{\boldsymbol{u}} = 0 \tag{1}$$

$$\boldsymbol{\sigma} \cdot \nabla + \rho \boldsymbol{b} = \rho \ddot{\boldsymbol{u}} \tag{2}$$

$$\rho \dot{e} = \boldsymbol{\sigma} : \dot{\boldsymbol{\epsilon}} + \rho s + \nabla \cdot \boldsymbol{q} \tag{3}$$

in which ρ is the current density, $\boldsymbol{u}$ is the displacement, $\boldsymbol{\sigma}$ is the Cauchy stress in the current configuration, $\boldsymbol{b}$ is the body force per unit mass, $\boldsymbol{\epsilon}$ is the strain tensor, s is the heat supply per unit mass and $\boldsymbol{q}$ is the heat flux vector per unit time and per unit area.

Many constitutive equations relate a stress-rate to a strain-rate or the rate of deformation as

$$\boldsymbol{\sigma}^{\nabla} = \boldsymbol{\sigma}^{\nabla}(\dot{\boldsymbol{\epsilon}}, \boldsymbol{\sigma}, \text{etc.}) \tag{4}$$

where $\boldsymbol{\sigma}^{\nabla}$ is the Jaumann rate of the Cauchy stress tensor defined by

$$\boldsymbol{\sigma}^{\nabla} = \dot{\boldsymbol{\sigma}} - \boldsymbol{\Omega} \cdot \boldsymbol{\sigma} - \boldsymbol{\sigma} \cdot \boldsymbol{\Omega}^{T} \tag{5}$$

where $\boldsymbol{\Omega}$ denotes the spin tensor. In the present work, the material constitutive equations of Jhonson-Cook model for metal and Holmquist-Johnson-Cook model for concrete are introduced as illustrated in Appendix A, together with the corresponding failure criterions.

Kinematic condition and boundary/initial conditions are summarized as follows:

$$\dot{\boldsymbol{\epsilon}} = \frac{1}{2}(\dot{\boldsymbol{u}} \cdot \nabla + \nabla \cdot \dot{\boldsymbol{u}}) \tag{6}$$

$$\begin{cases} \boldsymbol{n} \cdot \boldsymbol{\sigma} = \bar{\boldsymbol{t}}, & \boldsymbol{x} \in \Gamma_t \\ \boldsymbol{u} = \bar{\boldsymbol{u}}, & \boldsymbol{x} \in \Gamma_u \end{cases} \tag{7}$$

$$\dot{\boldsymbol{u}}(\boldsymbol{X}, 0) = \dot{\boldsymbol{u}}_0(\boldsymbol{X}), \quad \boldsymbol{u}(\boldsymbol{X}, 0) = \boldsymbol{u}_0(\boldsymbol{X}) \tag{8}$$

where Γ_t denotes the traction boundary, Γ_u denotes the displacement boundary, and $\boldsymbol{n}$ is the unit normal of the boundary Γ_t.

2.2. Euler equations for compressible flow

This paper focuses on the simulations of shock waves, and thus the flow dynamics considered here are governed by the compressible Euler equations

$$\frac{\partial \boldsymbol{U}}{\partial t} + \frac{\partial \boldsymbol{F}}{\partial x} + \frac{\partial \boldsymbol{G}}{\partial y} + \frac{\partial \boldsymbol{H}}{\partial z} = \boldsymbol{S} \tag{9}$$

where $\boldsymbol{S}$ is a general source term including the external force and body force, and $\boldsymbol{U}, \boldsymbol{F}, \boldsymbol{G}$ and $\boldsymbol{H}$ are in the conservative form as

$$\boldsymbol{U} = \begin{bmatrix} \rho \\ \rho u \\ \rho v \\ \rho w \\ \rho E \end{bmatrix}, \quad \boldsymbol{F} = \begin{bmatrix} \rho u \\ \rho u^2 + p \\ \rho uv \\ \rho uw \\ (\rho E + p)u \end{bmatrix}, \quad \boldsymbol{G} = \begin{bmatrix} \rho v \\ \rho uv \\ \rho v^2 + p \\ \rho vw \\ (\rho E + p)v \end{bmatrix}, \quad \boldsymbol{H} = \begin{bmatrix} \rho w \\ \rho uw \\ \rho vw \\ \rho w^2 + p \\ (\rho E + p)w \end{bmatrix} \tag{10}$$

where ρ is the fluid density, $[u, v, w]$ are flow velocities of x-, y- and z-direction, p is the flow pressure, and E is the total energy per unit mass. The ideal gas equation of state is used here to close the governing equations as

$$p = (\gamma - 1)\rho \left[E - \frac{1}{2}(u^2 + v^2 + w^2) \right] \tag{11}$$

3. Solid solver

3.1. Spatial discretization

Taking the virtual displacements $\delta \boldsymbol{u} \in \mathscr{R}_0, \mathscr{R}_0 = \left\{\delta \boldsymbol{u} | \delta \boldsymbol{u} \in C^0, \delta \boldsymbol{u}|_{\Gamma_u} = \boldsymbol{0}\right\}$, the weak form equivalent to momentum equation, Eq.(2), and traction boundary condition, Eq.(7), in updated Lagrangian formulation is given as

$$\int_\Omega \rho \ddot{\boldsymbol{u}} \cdot \delta \boldsymbol{u} \mathrm{d}V + \int_\Omega \boldsymbol{\sigma} : \delta \boldsymbol{\epsilon} \mathrm{d}V - \int_\Omega \rho \boldsymbol{b} \cdot \delta \boldsymbol{u} \mathrm{d}V - \int_{\Gamma_t} \bar{\boldsymbol{t}} \cdot \delta \boldsymbol{u} \mathrm{d}A = 0 \tag{12}$$

The MPM discretizes the material domain Ω into a set of Lagrangian particles moving through an Eulerian background grid, as shown in Fig.1. The particles act as quadrature points in calculating the integration in the weak form, and material density can be approximated with

$$\rho(\boldsymbol{x}) = \sum_{p=1}^{n_p} m_p \delta(\boldsymbol{x} - \boldsymbol{x}_p) \tag{13}$$

where n_p is the total number of particles, m_p is the mass of particle p, δ is the Dirac delta function with dimension of the inverse of particle volume, and $\boldsymbol{x}_p$ is the spatial coordinates of particle p.

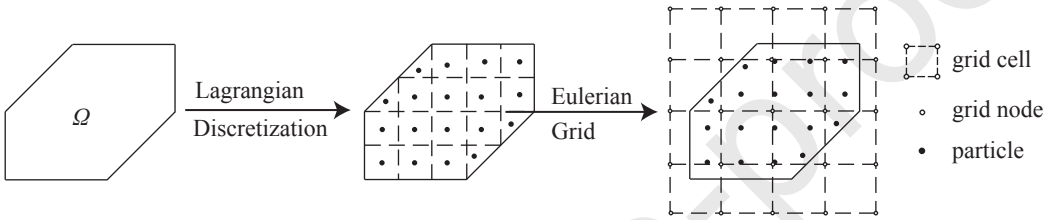

Figure 1: Standard MPM discretization

The displacement field $\boldsymbol{u}(\boldsymbol{x})$ of the computational domain is interpolated from the grid nodal displacement $\boldsymbol{u}_I$ by the shape function $N_I(\boldsymbol{x})$ of each grid node I, namely

$$\boldsymbol{u}(\boldsymbol{x}) = \sum_{I=1}^{n_g} N_I(\boldsymbol{x}) \boldsymbol{u}_I \tag{14}$$

where $N_I(\boldsymbol{x})$ is the linear/bilinear/trilinear shape function for standard MPM in 1D/2D/3D as that used in FEM.

Substituting Eqs. (13) and (14) into the weak form Eq.(12) leads to the discrete momentum equation at each grid point

$$\dot{\boldsymbol{p}}_I = \boldsymbol{f}_I^{\text{int}} + \boldsymbol{f}_I^{\text{ext}}, \quad \forall \boldsymbol{x}_I \notin \Gamma_u \tag{15}$$

in which

$$\boldsymbol{p}_I = m_I \dot{\boldsymbol{u}}_I \tag{16}$$

is the momentum at grid point I,

$$m_I = \sum_{p=1}^{n_p} m_p N_I(\boldsymbol{x}_p) \tag{17}$$

is the lumped grid mass matrix,

$$\boldsymbol{f}_I^{\text{int}} = -\sum_{p=1}^{n_p} \nabla N_{Ip} \cdot \boldsymbol{\sigma}_p \frac{m_p}{\rho_p} \tag{18}$$

and

$$\boldsymbol{f}_I^{\text{ext}} = \sum_{p=1}^{n_p} m_p N_{Ip} \boldsymbol{b}_p + \sum_{p=1}^{n_p} N_{Ip} \bar{\boldsymbol{t}}_p h^{-1} \frac{m_p}{\rho_p} \tag{19}$$

are the internal and external nodal forces with $\boldsymbol{\sigma}_p = \boldsymbol{\sigma}(\boldsymbol{x}_p)$ being the stress of particle p. In Eq.(19), h is the thickness of the fictitious layer used to convert the surface integral in the last term on the left side of Eq.(12) into a volume integral.

3.2. Temporal discretization

The leapfrog central difference integration scheme is used in the standard explicit MPM, which updates the position at integer time steps and the velocity at integer-plus-a-half time steps as

$$\boldsymbol{u}_I^{n+1} = \boldsymbol{u}_I^n + \Delta t^{n+1/2} \dot{\boldsymbol{u}}_I^{n+1/2} \tag{20}$$

$$\dot{\boldsymbol{u}}_I^{n+1/2} = \dot{\boldsymbol{u}}_I^{n-1/2} + \Delta t^n \ddot{\boldsymbol{u}}_I^n \tag{21}$$

where $\Delta t^{n+1/2} = t^{n+1} - t^n$ and $\Delta t^n = t^{n+1/2} - t^{n-1/2} = \frac{1}{2}(\Delta t^{n-1/2} + \Delta t^{n+1/2})$. $\boldsymbol{u}_I^{n+1}$ and $\boldsymbol{u}_I^n$ denote the displacement vectors at time t^{n+1} and t^n, $\dot{\boldsymbol{u}}_I^{n-1/2}$ denotes the velocity vector at time $t^{n-1/2}$.

3.3. MPM scheme

The stress state could be updated at the beginning of each time step, or at the end of each time step. The explicit MPM scheme with these two options is referred to as the update-stress-first (USF) scheme and the update-stress-last (USL). In the modified update-stress-last (MUSL) scheme, the grid nodal velocity obtained by mapping the updated particle momentum back to the grid nodes is used to update the stress. Different MPM schemes employ different grid nodal velocity fields to update the stress as shown in Fig.2.

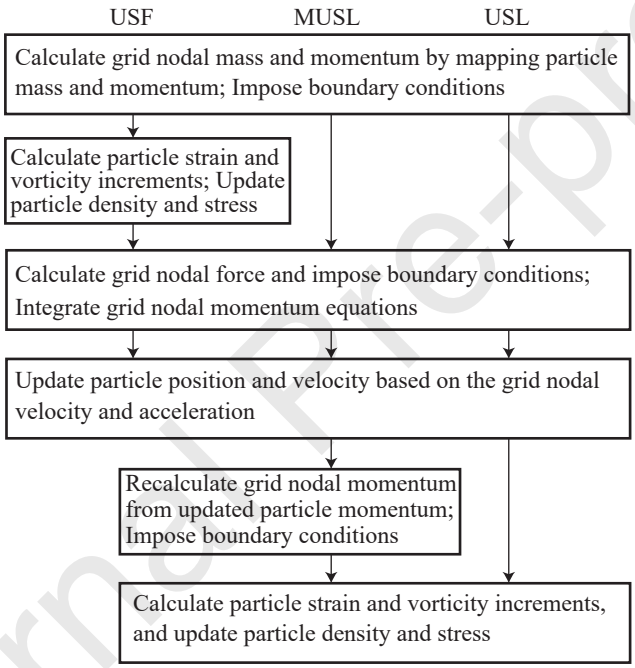

Figure 2: Flow chart of different MPM schemes [29]

Ni and Zhang [47] pointed out that both Lagrangian particle position and interaction between neighboring Eulerian grid cells will affect the simulation stability of MPM and the USL scheme suffers from an extremely small critical time step when cell-crossing phenomenon occurs. And, Bardenhagen [48] concluded that MUSL scheme tends to slowly dissipate energy while USF scheme tends to slowly increase in energy. The characteristic of energy increasing in USF scheme will lead to non-physical oscillation in the propagation of stress wave. Also, the numerical viscosity in MUSL scheme makes it more stable than USF scheme. Thus, the MUSL scheme is used in the present work.

4. Fluid solver

4.1. Spatial discretization

As shown in Fig.1, the background grid of MPM is discretized into structured Eulerian mesh which can be utilized for the spatial discretization of Euler equations, Eq.(9). And it is straightforward and convenient to apply

the immersed boundary conditions in IBM due to the utilization of the same Eulerian mesh. Finite volume method (FVM) is used to transform the conservation laws, Eq.(9), into the integral form

$$\frac{\mathrm{d}\bar{\boldsymbol{U}}_{i,j,k}(t)}{\mathrm{d}t}+\frac{1}{\Omega_{ijk}}[(\hat{\boldsymbol{F}}_{i+1/2,j,k}-\hat{\boldsymbol{F}}_{i-1/2,j,k})+(\hat{\boldsymbol{G}}_{i,j+1/2,k}-\hat{\boldsymbol{G}}_{i,j-1/2,k})+(\hat{\boldsymbol{H}}_{i,j,k+1/2}-\hat{\boldsymbol{H}}_{i,j,k-1/2})]=\bar{\boldsymbol{S}}_{i,j,k}(t) \quad (22)$$

where Ω_{ijk} is the volume of the grid cell $C_{ijk}=[x_{i-1/2},x_{i+1/2}]\times[y_{j-1/2},y_{j+1/2}]\times[z_{k-1/2},z_{k+1/2}]$,

$$\bar{\boldsymbol{U}}_{i,j,k}(t)=\frac{1}{\Omega_{ijk}}\int_{x_{i-1/2}}^{x_{i+1/2}}\int_{y_{j-1/2}}^{y_{j+1/2}}\int_{z_{k-1/2}}^{z_{k+1/2}}\boldsymbol{U}(x,y,z,t)\,\mathrm{d}x\mathrm{d}y\mathrm{d}z$$

is the spatial cell average of the conservative solution $\boldsymbol{U}(x,y,z,t)$ in the cell C_{ijk},

$$\hat{\boldsymbol{F}}_{i+1/2,j,k}=\int_{y_{j-1/2}}^{y_{j+1/2}}\int_{z_{k-1/2}}^{z_{k+1/2}}\boldsymbol{F}(x_{i+1/2},y,z,t)\,\mathrm{d}y\mathrm{d}z$$

is the flux at the grid cell surface $s_{i+1/2,j,k}=\{x=x_{i+1/2}\}\times[y_{j-1/2},y_{j+1/2}]\times[z_{k-1/2},z_{k+1/2}]$, $\hat{\boldsymbol{F}}_{i-1/2,j,k}$, $\hat{\boldsymbol{G}}_{i,j+1/2,k}$, $\hat{\boldsymbol{G}}_{i,j-1/2,k}$, $\hat{\boldsymbol{H}}_{i,j,k+1/2}$ and $\hat{\boldsymbol{H}}_{i,j,k-1/2}$ are the fluxes at the corresponding grid cell surfaces and take the similar form as $\hat{\boldsymbol{F}}_{i+1/2,j,k}$, and

$$\bar{\boldsymbol{S}}_{i,j,k}(t)=\frac{1}{\Omega_{ijk}}\int_{x_{i-1/2}}^{x_{i+1/2}}\int_{y_{j-1/2}}^{y_{j+1/2}}\int_{z_{k-1/2}}^{z_{k+1/2}}\boldsymbol{S}(x,y,z,t)\,\mathrm{d}x\mathrm{d}y\mathrm{d}z$$

is the spatial cell average of the general source term $\boldsymbol{S}(x,y,z,t)$ in the cell C_{ijk}.

A Riemann solver is used to calculate the flux terms for the simulations of shock wave. The procedure for evaluating the flux $\hat{\boldsymbol{F}}_{i-1/2,j,k}$ (other fluxes can be treated in the same way) is briefly summarized as follows:

1. The conservative solution $\bar{\boldsymbol{U}}_{i-1/2,j,k}=\bar{\boldsymbol{U}}(x_{i-1/2},y_j,z_k)$ at the center of cell surface $s_{i-1/2,j,k}$ is evaluated by linear reconstruction of cell center solutions $\bar{\boldsymbol{U}}_{i-1,j,k}$ and $\bar{\boldsymbol{U}}_{i,j,k}$, and it happens to be arithmetic average due to the structured Eulerian mesh, i.e.

$$\bar{\boldsymbol{U}}_{i-1/2,j,k}=\frac{1}{2}(\bar{\boldsymbol{U}}_{i-1,j,k}+\bar{\boldsymbol{U}}_{i,j,k}) \quad (23)$$

2. The MUSCL(Montone Upstream-Centered Scheme for Conservation Laws) interpolation is used to calculate the left state $\bar{\boldsymbol{U}}^L_{i+1/2,j,k}$ and the right state $\bar{\boldsymbol{U}}^R_{i-1/2,j,k}$ by a slope limiter in the grid cell C_{ijk}

$$\bar{\boldsymbol{U}}^L_{i+1/2,j,k}=\bar{\boldsymbol{U}}_{i,j,k}+\frac{1}{2}\mathrm{limiter}(2\Delta\bar{\boldsymbol{U}}^L_{i+1/2,j,k},\,2\Delta\bar{\boldsymbol{U}}^R_{i-1/2,j,k}) \quad (24)$$

$$\bar{\boldsymbol{U}}^R_{i-1/2,j,k}=\bar{\boldsymbol{U}}_{i,j,k}-\frac{1}{2}\mathrm{limiter}(2\Delta\bar{\boldsymbol{U}}^R_{i-1/2,j,k},\,2\Delta\bar{\boldsymbol{U}}^L_{i+1/2,j,k}) \quad (25)$$

in which limiter$(x,\,y)$ is the slope limiter function and in this paper takes the formulation as Venkatakrishnan [49]

$$\mathrm{limiter}(x,\,y)=\frac{1}{2}\left|\mathrm{sign}(x)+\mathrm{sign}(y)\right|\frac{x(y^2+2\epsilon^2)+y(2x^2+\epsilon^2)}{2x^2-xy+2y^2+3\epsilon^2}$$

where ϵ is an infinitesimal to avoid zero in denominator, and

$$\Delta\bar{\boldsymbol{U}}^L_{i+1/2,j,k}=\bar{\boldsymbol{U}}_{i+1/2,j,k}-\bar{\boldsymbol{U}}_{i,j,k}$$

$$\Delta\bar{\boldsymbol{U}}^R_{i-1/2,j,k}=\bar{\boldsymbol{U}}_{i,j,k}-\bar{\boldsymbol{U}}_{i-1/2,j,k}$$

3. The Lax-Friedrichs flux $\boldsymbol{F}_{i-1/2,j,k}$ is calculated based on the left and right states at the center of grid cell surface $s_{i-1/2,j,k}$

$$\boldsymbol{F}_{i-1/2,j,k}=\frac{1}{2}[\boldsymbol{F}(\bar{\boldsymbol{U}}^L_{i-1/2,j,k})+\boldsymbol{F}(\bar{\boldsymbol{U}}^R_{i-1/2,j,k})-\alpha(\bar{\boldsymbol{U}}^R_{i-1/2,j,k}-\bar{\boldsymbol{U}}^L_{i-1/2,j,k})] \quad (26)$$

where $\alpha=\max_{\boldsymbol{U}}|\partial\boldsymbol{F}(\boldsymbol{U})/\partial\boldsymbol{U}|=\max(|u^L_n|,\,|u^R_n|)+\max(a^L,\,a^R)$, u^L_n and u^R_n are the normal velocity of left and right state respectively on the surface $s_{i-1/2,j,k}$, and a^L and a^R are the sound speed of left and right state respectively on the surface $s_{i-1/2,j,k}$.

4. Single-point Gaussian integral is used to calculate the flux $\hat{\boldsymbol{F}}_{i-1/2,j,k}$ at the grid cell surface $s_{i-1/2,j,k}$

$$\hat{\boldsymbol{F}}_{i-1/2,j,k}=\boldsymbol{F}_{i-1/2,j,k}\cdot\mathrm{Area}(s_{i-1/2,j,k}) \quad (27)$$

4.2. Temporal discretization

In order to be consistent with the velocity $\dot{\boldsymbol{u}}_I^{n+1/2}$ of solid structure in MPM to apply the immersed boundary conditions, the conservative solutions of flow are also defined at integer-plus-a-half time steps as $\bar{\boldsymbol{U}}^{(n+1/2)}$. The integral form of Euler equations can be rewritten into semi-discrete format by moving the flux terms of Eq.(22) to the right hand as

$$\frac{\mathrm{d}\bar{\boldsymbol{U}}}{\mathrm{d}t} = \mathrm{RHS}(\bar{\boldsymbol{U}}^{(n-1/2)}) \tag{28}$$

The third-order TVD Runge–Kutta method is used for temporal discretization

$$\begin{aligned}
\bar{\boldsymbol{U}}^{(n-1/2,1)} &= \bar{\boldsymbol{U}}^{(n-1/2)} + \Delta t \cdot \mathrm{RHS}(\bar{\boldsymbol{U}}^{(n-1/2)}) \\
\bar{\boldsymbol{U}}^{(n-1/2,2)} &= \frac{3}{4}\bar{\boldsymbol{U}}^{(n-1/2)} + \frac{1}{4}[\bar{\boldsymbol{U}}^{(n-1/2,1)} + \Delta t \cdot \mathrm{RHS}(\bar{\boldsymbol{U}}^{(n-1/2,1)})] \\
\bar{\boldsymbol{U}}^{(n+1/2)} &= \frac{1}{3}\bar{\boldsymbol{U}}^{(n-1/2)} + \frac{2}{3}[\bar{\boldsymbol{U}}^{(n-1/2,2)} + \Delta t \cdot \mathrm{RHS}(\bar{\boldsymbol{U}}^{(n-1/2,2)})]
\end{aligned} \tag{29}$$

in which $\bar{\boldsymbol{U}}^{(n-1/2,k)}$ is the conservative solutions of the k-th Runge–Kutta loop at the time step $n-1/2$.

5. IB method for shock-structure interaction

In the present work, immersed boundary method (IBM) is adopted to couple the MPM solver in Section 3 and the FVM Riemann solver in Section 4 for the interaction between fluid and solid. Traditional continuous forcing approach of IBM is implemented in a sense of penalty function method, and the slip or non-slip boundary conditions can not be satisfied strictly at each time step. When simulating shock-structure interaction problems, shock structures sensitive to boundary velocity direction, such as Mach reflection, may vanish. Traditional discrete forcing approach of IBM needs to calculate normal directions and vertical distances along the immersed boundary at each time step, which is time-consuming. Moreover, in the dynamic fracture simulations, small fragments of thin geometry and fresh FSI interfaces will be generated, which makes the FSI interface difficult to be reconstructed.

To avoid the above mentioned shortcomings of two approaches in simulating shock-structure interaction and accompanied dynamic fracture, a novel Lagrangian continuous-forcing IBM (lg-CFIBM) is proposed by combining the concepts of GCIB method and penalty IB method. The lg-CFIBM is implemented in the frame of continuous forcing approach with a compact support area for the immersed boundary conditions. It can guarantee the boundary velocity conditions strictly at each time step and has no need to reconstruct FSI interfaces, which makes it a promising method for the simultaneous simulations of shock-structure interaction and accompanied dynamic fracture.

As FSI interface is not tracked during the simulation in lg-CFIBM, the immersed boundary needs to be located for boundary condition imposition at each time step. A two-step grid cell classification algorithm is developed in the Section 5.1 to find the grid cells where the immersed boundary locates. And then, the specific formulations of immersed boundary conditions in lg-CFIBM are given in Section 5.2.

5.1. Grid cell classification

In order to impose the fluid-structure boundary conditions, the position of the immersed boundary needs to be located first. As shown in Fig.3, the grid cells embedded in the solid structure are classified as "Cell Type I", the grid cells submerged in the fluid flow are classified as "Cell Type II" and the grid cells where the immersed boundary locates are classified as "Cell Type III". Typically, the nodes of cell type I and of cell type II are all inside the same material phase, in solid or in fluid individually, and the nodes of cell type III are always of different material phases. However, special cases for cell type III will occur as shown in Fig.4 when the solid structure is of thin geometry or there exists isolated material particles in dynamic fracture simulations.

The movement of solid structure is tracked by the Lagrangian particles in MPM. And, the immersed boundaries of red lines with square mark in Figs.3 and 4 are just for illustration. With the definition of the immersed boundary $\Gamma_{ib} = \partial\Omega_\mathrm{s},\ \Omega_\mathrm{s} = \bigcup_{p=1}^{n_p}\Omega_p$ where Ω_p is the volume of particle p, the grid cells can be classified by the distribution of particles without knowing the exact positions of the immersed boundaries.

The classification of grid cells is carried out by the following two steps:

1. Identify which grid cell each particle is located in and preliminarily classify the grid cells into two categories, occupied cell with particles in it and vacuum cell without any particle. And those vacuum cells are of type II.

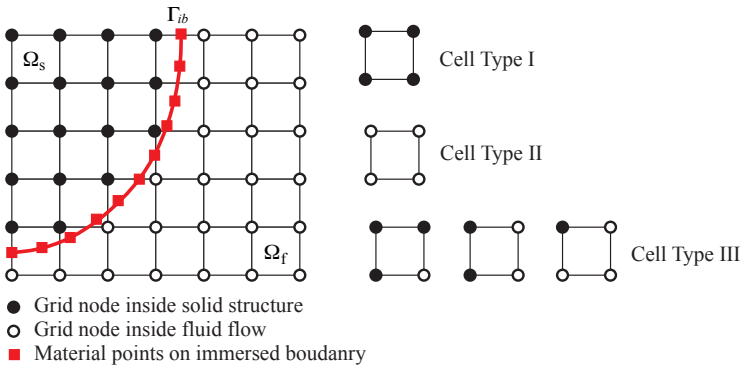

Figure 3: Grid cell classification

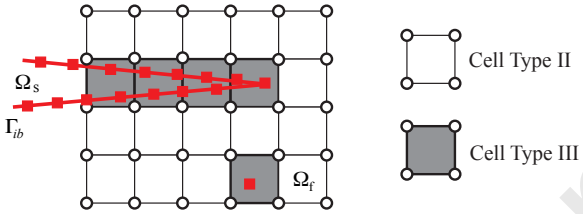

Figure 4: Special cases of thin geometry of structure and isolated material particles

2. Search the neighboring cells ($3 \times 3 \times 3 = 27$ cells in 3-dimension) of each occupied cell. If all the neighboring cells are occupied cells, then this occupied cell is of type I. Otherwise, this occupied cell is of type III.

And fortunately, with the above procedure, special cases of thin geometry and isolated material particles will be automatically classified into cell type III.

5.2. Immersed boundary methods

In this section, the procedures of ghost-cell immersed boundary (GCIB) method and continuous forcing IBM (also known as penalty IBM) will be briefly reviewed and the shortcomings of these procedures for shock-structure interaction and accompanied dynamic fracture simulations will also be illustrated. And then, a novel IBM combining the advantages of discrete forcing IBM and continuous forcing IBM will be proposed in detail. Fig.5 shows the core ideas of these IBMs, ① for GCIB method, ② for penalty IBM and ③ for the lg-CFIBM.

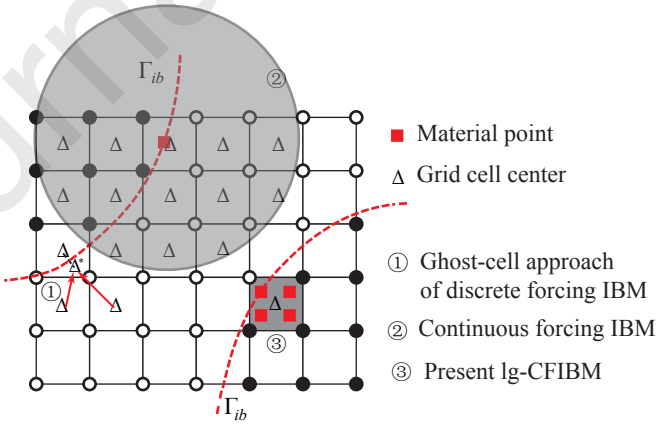

Figure 5: Diagram of applying boundary conditions of different IBMs

5.2.1. GCIB method

In GCIB method, the boundary velocity conditions are applied at the center of type III cells. As shown in Fig.5①, the corresponding image point Δ^* is required for each ghost point Δ (center of type III cells) orthogonal

to the boundary, and the flow state at the image point is reconstructed by the surrounding fluid cell center state $\bar{\boldsymbol{U}}_{i,j,k}$. And then, a linear approximation is used to calculate the flow state at each ghost point based on the flow state of the corresponding image point and the velocity of immersed boundary. The boundary force conditions are imposed on solid structures by integrating the pressure along the immersed boundary. In the application of both the boundary velocity conditions and the boundary force conditions, the normal directions of the immersed boundary are demanded, which means that the exact position of fluid-structure interface needs to be tracked and reconstructed at each time step. And thus, to our best knowledge, there are few works applying the discrete forcing IBMs (including GCIB method) to the simultaneous simulations of shock-structure interaction and accompanied dynamic fracture, in which the topology of the fluid-structure interface will heavily change.

5.2.2. Penalty IB method

In the penalty IBM as shown in Fig.5②, each particle on the immersed boundary is associated with a mass-less Lagrangian point which undergoes the same velocity field of fluid flow and drags the particle back by the feedback force as

$$\boldsymbol{F} = \kappa_1 \left[\int_0^t (\boldsymbol{v}_{ib} - \boldsymbol{v}) \, \mathrm{d}t + \Delta t \, (\boldsymbol{v}_{ib} - \boldsymbol{v}) \right], \quad \text{or just } \boldsymbol{F} = \kappa_2 \, (\boldsymbol{v}_{ib} - \boldsymbol{v})$$

where $\boldsymbol{v}_{ib}$ is the velocity of particle on the immersed boundary, κ_1, κ_2 are the corresponding penalty coefficients and the velocity of the mass-less point takes the formulation as

$$\boldsymbol{v} = \int_\Omega \boldsymbol{v}_\mathrm{f} \cdot \delta(\boldsymbol{x} - \boldsymbol{x}_{ib}) \, \mathrm{d}\boldsymbol{x}$$

where $\boldsymbol{v}_\mathrm{f}$ is the velocity field of fluid flow and $\boldsymbol{x}_{ib}$ is the position of particle on the immersed boundary. Obviously, the feedback law is implemented in a sense of penalty function method and cannot satisfy the boundary velocity conditions strictly. Moreover, a smoothed approximation of the Dirac delta function $\delta(\boldsymbol{x} - \boldsymbol{x}_{ib})$ is used in the reconstruction of mass-less point velocity and Lagrangian/Eulerian force transformation, which will cause non-physical oscillations around the discontinuity in the simulations of shock waves due to its large support area shown as the gray circle in Fig.5. When coupling with MPM, all the particles in the grid cells of type III are identified as on the immersed boundary, and typically there are two particles per cell in each direction ($2 \times 2 \times 2 = 8$ particles in each grid cell for 3-dimension) to prevent numerical fracture phenomenon. And the diameter of the Dirac delta function support area is typically of 5 grid cells. Because the number of particles on the immersed boundary (about 8 times the amount of the type III cells) is larger than the number of grid cell centers in the support area (about 5 times the amount of the type III cells), the system will be of over-constraint which will also cause non-physical oscillations. The above mentioned shortcomings lead to the vanish of some shock structures which are sensitive to flow velocity direction, such as Mach reflection.

5.2.3. Lagrangian Continuous-Forcing IB method (lg-CFIBM)

In order to avoid the reconstruction of the fluid-structure interface, a Lagrangian Continuous-Forcing IB method is proposed in the frame of the continuous forcing IBM. In the penalty IBM, the boundary velocity conditions are imposed on the Lagrangian particles of the immersed boundary which will leads to an over-constraint system in penalty function method as illustrated in Section 5.2.2. Therefore, in the proposed lg-CFIBM, the boundary velocity conditions are imposed at the center of type III cells like GCIB method. In GCIB method, the velocity at the center of type III cell is reconstructed by the first order extrapolation at the normal direction of the immersed boundary, while in the present lg-CFIBM the zero order extrapolation is adopted to avoid the use of normal direction. That is, with the momentum $\boldsymbol{p}_I$ and lumped mass m_I of grid node I reconstructed by the particles in Eqs. (16) and (17), the immersed boundary velocity $\boldsymbol{v}_c^{ib}$ of solid structure at the center of type III cell c is given as

$$\boldsymbol{v}_c^{ib} = \sum_{I=1}^{n_\mathrm{en}} \frac{1}{n_\mathrm{en}} \cdot \frac{\boldsymbol{p}_I}{m_I} \tag{30}$$

where n_en is the node number of each cell and equals 2/4/8 for structured grid in 1D/2D/3D individually. By setting the fluid velocity $\boldsymbol{v}_c$ of the type III cell c to be the immersed boundary velocity $\boldsymbol{v}_c^{ib}$ and solving the Euler equations, the immersed boundary velocity conditions can be satisfied strictly at each time step.

The imposition of the immersed boundary velocity conditions, Eq.(30), is equivalent to imposing an Eulerian forcing term in the cell c of type III at the end of each Runge-Kutta loop as

$$\boldsymbol{f}_c^k = -\frac{\rho_c^k (\Delta \boldsymbol{v})_c^k}{\Delta t}, \; k = \{1, 2, 3\} \tag{31}$$

where ρ_c^k is the cell center density and $(\Delta \boldsymbol{v})_c^k = \boldsymbol{v}_c^k - \boldsymbol{v}_c^{ib}$ is the difference between the cell center velocity $\boldsymbol{v}_c^k$ and the immersed boundary velocity $\boldsymbol{v}_c^{ib}$ of cell c at the end of k-th Runge-Kutta loop. In lg-CFIBM, the grid cells of type III act as ghost cells. Thus, the flow states are not recorded and only the surface fluxes are calculated. With the equality of total differential $\Delta(\rho \boldsymbol{v}) = \rho \Delta \boldsymbol{v} + \boldsymbol{v} \Delta \rho$, the Eulerian forcing term of Eq.(31) can be rewritten into

$$\boldsymbol{f}_c^k = -\frac{(\Delta(\rho \boldsymbol{v}))_c^k - \boldsymbol{v}_c^{ib}(\Delta \rho)_c^k}{\Delta t} = \alpha^k \left(\boldsymbol{v}_c^{ib} \mathrm{RHS}_c^k(\rho) - \mathrm{RHS}_c^k(\rho \boldsymbol{v}) \right) \tag{32}$$

where $(\Delta \rho)_c^k = \alpha^k \Delta t \mathrm{RHS}_c^k(\rho)$ and $(\Delta(\rho \boldsymbol{v}))_c^k = \alpha^k \Delta t \mathrm{RHS}_c^k(\rho \boldsymbol{v})$ are respectively the increments of mass and momentum caused by surface fluxes of cell c in the k-th Runge-Kutta loop and $\alpha^k \in \{1,\ 1/4,\ 2/3\}$ is the coefficient of the k-th Runge-Kutta loop as in Eq.(29).

Based on the conservation law of momentum, the reaction force of the Eulerian forcing term needs to be imposed on the solid structure. As all the particles in the cell c of type III are identified as on the immersed boundary, the reaction force is evenly distributed onto these particles by

$$\boldsymbol{F}_p^k = -\frac{1}{n_p^c} \boldsymbol{f}_c^k V_c \tag{33}$$

in which $\boldsymbol{F}_p^k$ is the reaction force on the particle p in the cell c at k-th Runge-Kutta loop, n_p^c is the number of particles in the cell c and V_c is the volume of cell c. According to the coefficients of the third order TVD Runge-Kutta method in Eq.(29), the total reaction force $\boldsymbol{F}_p$ on the particle p of each time step is given as

$$\boldsymbol{F}_p = \frac{1}{6} \boldsymbol{F}_p^1 + \frac{2}{3} \boldsymbol{F}_p^2 + \boldsymbol{F}_p^3 \tag{34}$$

In addition, the grid cells of type III also serve as the fictitious layer to calculate the surface integral of the traction $\bar{\boldsymbol{t}}$ on the fluid-structure interface in Eq.(19). By replacing the term $\bar{\boldsymbol{t}}_p h^{-1} m_p / \rho_p$ with $\boldsymbol{F}_p$, the external nodal forces in MPM are given as

$$\boldsymbol{f}_I^{\mathrm{ext}} = \sum_{p=1}^{n_p} m_p N_{Ip} \boldsymbol{b}_p + \sum_{p=1}^{n_p} N_{Ip} \boldsymbol{F}_p \tag{35}$$

In lg-CFIBM, the imposition of the boundary force condition on solid structures is implemented in the frame of the continuous forcing approach according to the conservation law of momentum. And it has no need to integrate the pressure tensor along the immersed boundary which requires the normal direction. Therefore, the lg-CFIBM does not have to reconstruct the FSI interface and is suitable for dynamic fracture simulations where small fragments of thin geometry and fresh FSI interfaces will be generated. Furthermore, the immersed boundary velocity conditions can be satisfied strictly at each time step in lg-CFIBM. Thus, the lg-CFIBM is capable for the shock-structure interaction, especially Mach reflection which is sensitive to the boundary velocity direction.

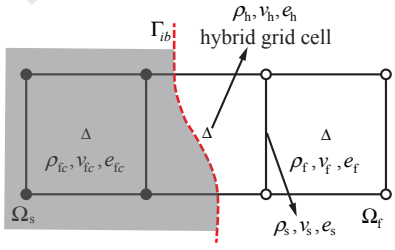

Figure 6: Diagram of modified linear reconstruction

The phenomenon of mass penetration from fluid to solid is a common problem in all the IBMs. The treatment in lg-CFIBM is much like GCIB method. As shown in Fig.6, the fictitious fluid embedded in the solid structure is of density $\rho_{\mathrm{f}c}$, velocity field $\boldsymbol{v}_{\mathrm{f}c}$ and internal energy $e_{\mathrm{f}c}$, and the real fluid is of density ρ_{f}, velocity field $\boldsymbol{v}_{\mathrm{f}}$ and internal energy e_{f}. In lg-CFIBM, the fictitious fluid is not simulated in Euler equations and the hybrid grid cell is occupied only by the real fluid. Thus, the density ρ_{h} and the internal energy e_{h} of the hybrid grid cell are reconstructed by the neighboring fluid cells of type I to prevent the mass penetration into solid as

$$\rho_{\mathrm{h}} = \rho_{\mathrm{f}}, \quad e_{\mathrm{h}} = e_{\mathrm{f}}, \quad \boldsymbol{v}_{\mathrm{h}} = \boldsymbol{v}^{ib} \tag{36}$$

5.3. Algorithm Summary and Remark

The overall computation process of the present numerical algorithm, called IBMPM, at each time step for simulating the shock-structure interaction and accompanied dynamic fracture is summarized as follows:

(***Time-Step Loop***)

1. Calculate grid nodal mass and momentum by mapping particle mass and momentum, Eqs.(16) and (17). Impose boundary conditions for solid structure.
2. Classify the grid cells into type I, II and III according to the distribution of particles.
   (***Runge-Kutta Loop***)
   (a) Reconstruct the density and internal energy at the center of type III cells by the neighboring type I cells.
   (b) Carry out the processes of Riemann solver, Eqs.(23)-(27), and update the flow states at the cell center, Eq.(28).
   (c) Apply the immersed boundary velocity conditions to the cell center of type III, Eq.(30), and calculate the reaction force, Eqs.(32) and (33).
3. Calculate the total reaction force with different coefficients for each Runge-Kutta loop, Eq.(34), and apply the reaction force to the particles in grid cells of type III, Eq. (35).
4. Carry out the rest processes of MUSL scheme MPM as shown in Fig.2.

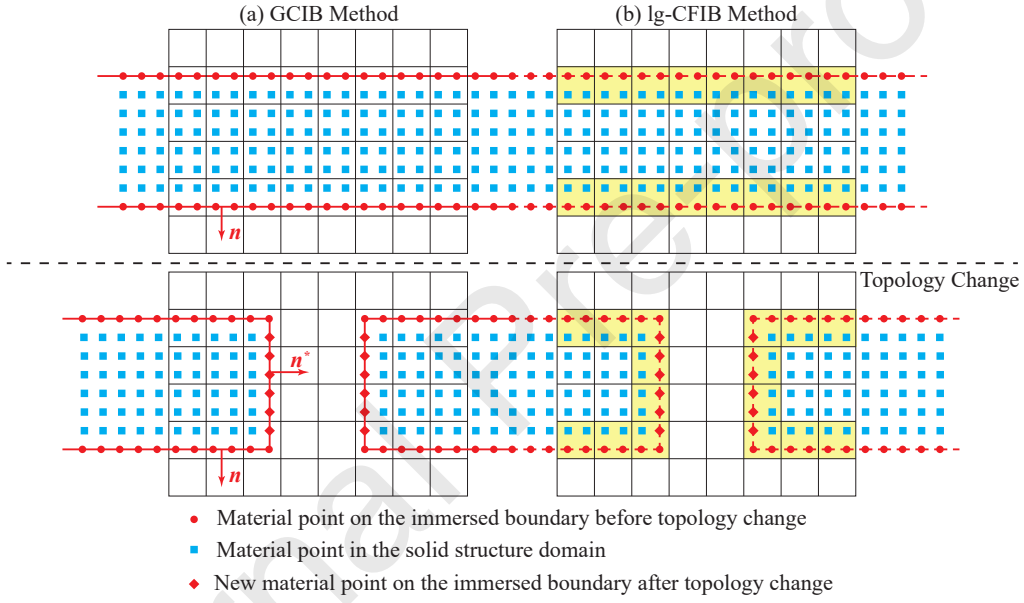

Figure 7: Comparison between the immersed boundary treatments in GCIB method and lg-CFIBM

Remark 1: In the GCIB method, the FSI interfaces need to be tracked and reconstructed by segments of 2D or triangular patches of 3D to calculate normal direction, $\boldsymbol{n}$ and $\boldsymbol{n}^*$ as shown in Fig.7(a), along the immersed boundary. In the simulation of dynamic fracture, the topology of solid structure will heavily change and there will be a lot of freshly generated FSI interfaces. That means, we need to identify and reconstruct the FSI interfaces by triangular patches at each time step. Furthermore, the identification of which material point is on the fresh FSI interfaces and the surface reconstruction process of these material points cloud in 3D space are difficult, unstable and time-consuming.

In the lg-CFIBM, we also need to track and locate the FSI interfaces to apply the immersed boundary conditions. However, only the information of which grid cell FSI interfaces go through is demanded as shown in Fig.7(b), which is much easier to obtain than the accurate position of FSI interfaces in GCIB method. On the other hand, there is no need to calculate the normal direction along the FSI interfaces. Therefore, the surface reconstruction process is no longer needed in our lg-CFIBM. So, lg-CFIBM is a promising method to simulate the fluid-structure interaction when the solid structures undergo extreme deformation and heavy topology change.

Remark 2: As mentioned in Section 5.2.3, the zero order extrapolation is adopted in Eq.(30) to avoid the calculation of normal direction along the surface of solid structure. The zero order extrapolation treatment turns

out to be the application of no-slip boundary condition around the immersed boundary. However, the flow dynamics are governed by the Euler equations and the boundary velocity condition is only applied on the ghost cells of type III. Therefore, the difference in the tangential velocities near the immersed boundary will not spread into the real fluid domain with the absence of viscosity. That is, the zero order extrapolation is a reasonable method to apply the slip boundary condition near the immersed boundary in the present work. And as shown in the numerical results in Section 6.3 and Section 6.4, the IBMPM with the zero order extrapolation can capture the Mach reflection very well which is sensitive to the boundary velocity direction. Furthermore, it will be a straightforward method to ensure no-slip boundary condition if the viscosity and shear forces are considered.

6. Numerical results

In this section, convergence rates of solid structure solver and fluid solver are measured analytically by 1D string vibration problem and 2D vortex evolution problem individually. And then, the capacity of the immersed boundary-material point method (IBMPM) to simulate shock-structure interaction will be verified by simulations of shock/cylinder interaction and flexible panel deformation induced by a shock wave. And the numerical results will be compared with the published experiment results. Finally, the IBMPM is applied to simulate the fragmentation of cylinder shell and sphere shell induced by explosive detonation.

6.1. 1D string vibration

Our laboratory code, MPM3D, is used for MPM solver and its correctness and capacity in simulating extreme deformation problem have been verified these years[29–39,42,47]. And here, a simple 1D string vibration shown in Fig.8(a) is presented to evaluate the convergence rate of MPM solver. It has an analytical solution in small deformation. If the initial velocity condition and boundary conditions are given as

$$v\left(x,0\right)=v_0\sin\left(\frac{\pi x}{L}\right),\quad u\left(0,t\right)=u\left(L,t\right)=0 \tag{37}$$

then the analytical displacement solution is

$$u\left(x,t\right)=\frac{v_0 L}{\pi}\sqrt{\frac{\rho}{E}}\sin\left(\omega t\right)\sin\left(\frac{\pi x}{L}\right) \tag{38}$$

where v_0 is the amplitude of velocity, E is the Young's modulus, ρ is the material density and L is the total length of string.

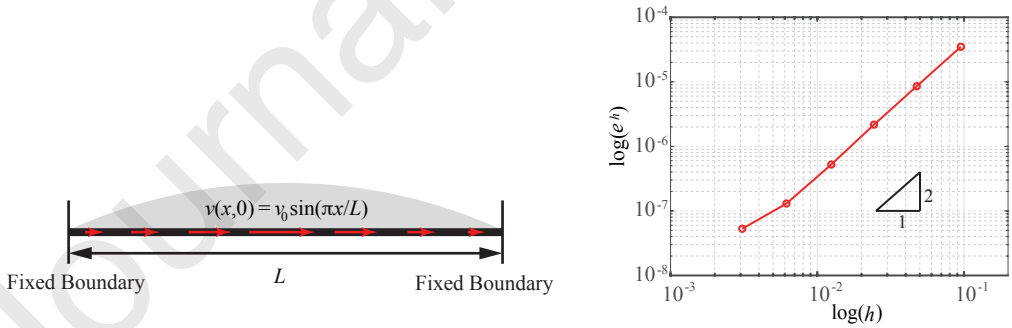

(a) Diagram for 1D string

(b) Log-log plot of error v.s. cell size

Figure 8: 1D string vibration test for MPM solver

The amplitude of velocity is set to $v_0=0.1\,\mathrm{m/s}$ which satisfy the small deformation assumption. The material has a density of $\rho=25\,\mathrm{kg/m^3}$, Young's modulus of $E=50\,\mathrm{Pa}$ and Poisson's rate $\nu=0$. The following L_2-norm error of a specific cell size h is defined by the particle quadrature to evaluate the convergence rate

$$e^h=\sqrt{\int_0^L\left(u^h(x,t)-u(x,t)\right)^2\,\mathrm{d}x}=\sqrt{\sum_{p=1}^{n_p}\left(u_p^h(t)-u_p(t)\right)^2} \tag{39}$$

where $u_p^h(t) = u^h(x_p, t)$ and $u_p(t) = u(x_p, t)$. The whole string is discretized into $10, 20, 40, 80, 160$ and 320 cells, and there are 2 particles in each cell for all cases. The above L_2-norm error is evaluated at $t = 0.02\,\mathrm{s}$ and a small time step size of $\Delta t = 10^{-5}\,\mathrm{s}$ is used for all cases. As shown in the log-log plot of error verses cell size in Fig.8(b), the convergence rate of MPM, which is the slope of the line, is very close to 2.

6.2. 2D vortex evolution

Toro[50] used the 2D vortex evolution problem to study the convergence properties of finite-difference WENO schemes for Euler equations. The same initial condition and boundary conditions are used to evaluate the convergence rate of the Riemann solver in the present work.

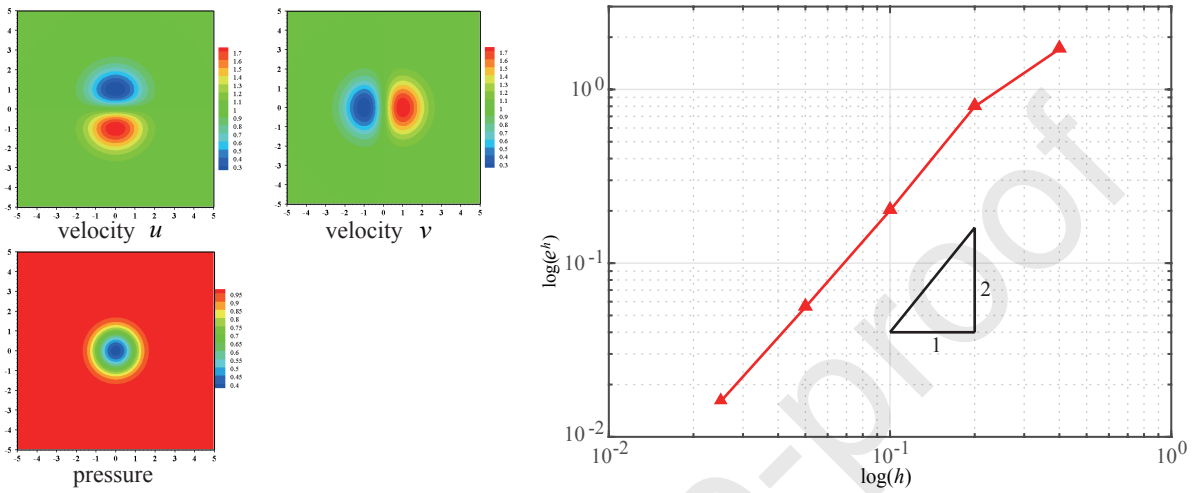

(a) Initial conditions of 2D vortex

(b) Log-log plot of error v.s. cell size

Figure 9: 2D vortex evolution test for Riemann solver

As shown in Fig.9(a), the problem is solved in the square domain of $[-5, 5] \times [-5, 5]$ with periodic boundary conditions. The initial conditions of vortex is defined as the isentropic perturbation to the uniform flow of unit values of primitive variables:

$$u(x,y) = 1 - \frac{\epsilon y}{2\pi}\exp\left(\frac{1}{2}(1-x^2-y^2)\right), \quad v(x,y) = 1 + \frac{\epsilon x}{2\pi}\exp\left(\frac{1}{2}(1-x^2-y^2)\right)$$

$$T(x,y) = 1 - \frac{(\gamma-1)\epsilon^2}{8\gamma\pi^2}\exp\left(1-x^2-y^2\right), \quad \frac{p}{\rho^\gamma} = 1 \tag{40}$$

where the vortex strength $\epsilon = 5$. The following L_2-norm error of a specific cell size h is calculated at the end of time $t = 10$ which equals one time period by the single Gaussian quadrature of grid cell center

$$e^h = \sqrt{\int_\Omega [(u^h(x,y) - u(x,y))^2 + (v^h(x,y) - v(x,y))^2]\mathrm{d}\Omega} = \sqrt{\sum_{c=1}^{n_c}[(u_c^h - u_c)^2 + (v_c^h - v_c)^2]} \tag{41}$$

in which $u^h(x,y)$ and $v^h(x,y)$ are the numerical results of cell size h, and $(\cdot)_c = (\cdot)(x_c, y_c)$. As shown in Fig.9(b), the Riemann solver implemented in the present work has the convergence rate of 2.

6.3. Shock-cylinder obstacle interaction

Shock-cylinder obstacle interaction is a classical and well studied test case in the literature. Chaudhuri[22] used this test case to verify the ability of GCIB method in simulating shock-structure interaction. The initial flow states of the computational domain are set the same as Lomax[51] as shown in Fig.10(a). And the published experiment results from Gross[52] are shown in Fig.10(b).

The flow conditions ahead of (ρ_1, u_1, p_1) and behind (ρ_2, u_2, p_2) a moving shock are related by

$$\frac{p_2}{p_1} = \frac{2\gamma M_S^2 - (\gamma-1)}{\gamma+1}, \quad \frac{\rho_2}{\rho_1} = \frac{(\gamma+1)p_2 + (\gamma-1)p_1}{(\gamma+1)p_1 + (\gamma-1)p_2}, \quad u_2 = M_S\left[1 - \frac{(\gamma-1)M_S^2+2}{(\gamma+1)M_S^2}\right]c_1 \tag{42}$$

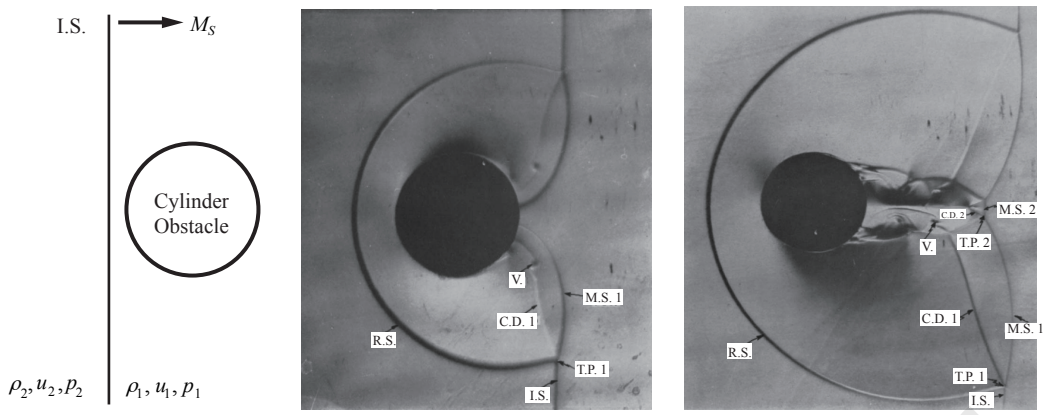

(a) Initial position of I.S.

(b) Experiments results for shock structures (Gross 1961)

Figure 10: Shock-cylinder obstacle interaction problem at $M_S = 2.81$. (a) initial position of I.S. (b) published experiment results from Gross[52]. (I.S. = incident shock, R.S. = reflected shock, M.S. = mach shock, C.D. = contact discontinuity, T.P. = triple point, V. = vortex)

in which M_S is the mach number of I.S. moving speed, $c_1 = \sqrt{\gamma p_1/\rho_1}$ is the sound speed of flow ahead of I.S.. The non-dimensional initial flow states ahead of I.S. are of density $\rho_1 = 1$, pressure $p_1 = 1$, velocity $u_1 = 0$ and $v_1 = 0$, and the initial flow states behind I.S. can be calculated by Eq.(42) with $M_S = 2.81$ and $\gamma = 1.4$. The problem is simulated in the non-dimensional domain of $[-1.5, 5] \times [-5, 5]$ with the cell size $h = 0.0025$. The boundary condition at $x = -1.5$ is inlet condition of flow states ρ_2, u_2, p_2, and that at $x = 5$ is outlet condition while others are set rigid wall boundary conditions. The cylinder obstacle of non-dimensional diameter $D = 1$ is a fixed rigid body and set at the origin [0, 0], and is discretized by particles with the volume of 0.00125×0.00125. The initial position of the I.S. is located to the left of the cylinder at $x = -0.6$.

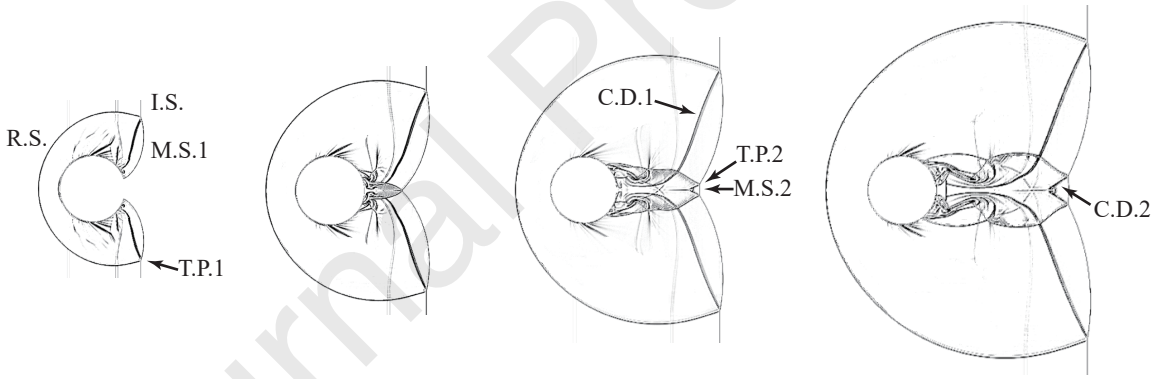

(a) $t = 0.4$ (b) $t = 0.6$ (c) $t = 0.8$ (d) $t = 1.0$

Figure 11: Numerical shadowgraph of IBMPM for shock-cylinder obstacle interaction problem

The details of the transient shock wave diffraction phenomena are shown in Fig.11. Comparing the numerical results of $t = 0.4$ and $t = 0.8$, Figs.11(a) and (c), with the experiment results in Fig.10(b), the proposed IBMPM reproduces the diffraction process correctly, such as regular reflection (R.S.), transition to Mach reflection (M.S.1 and M.S.2), complex weak/shock (C.D.1 and C.D.2) and shock/shock interactions (T.P.1 and T.P.2). The trajectories of the Mach shock triple points T.P.1 and T.P.2 are depicted in the Fig.12. Compared with the experiment data from Gross[52] and numerical results of Chaudhuri[22], our IBMPM gives satisfactory numerical results for T.P.1 and T.P.2.

As a summary, the imposition of immersed boundary velocity condition in the lg-CFIBM is verified by the correct reproduction of diffraction process, especially the Mach reflection which is sensitive to the velocity direction, and our IBMPM has the ability to simulate the shock-stationary obstacle interaction.

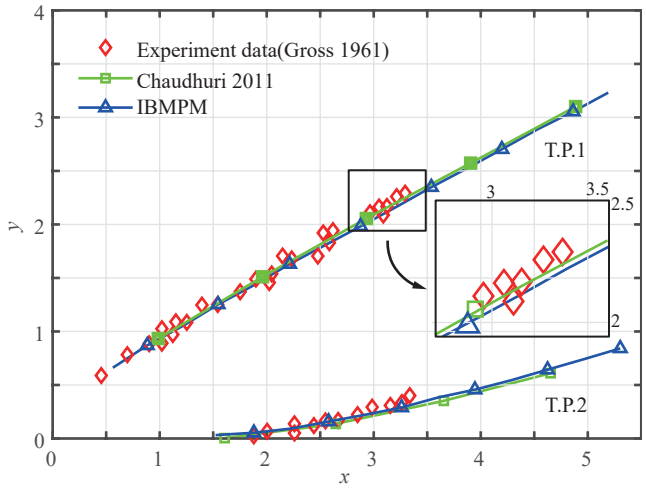

Figure 12: Trajectories of the Mach shock triple points T.P.1 and T.P.2

6.4. Flexible panel deformation induced by shock wave

In this section, the deformation of flexible panel induced by shock wave will be simulated to verify the procedure of immersed boundary force condition in the lg-CFIBM. The experiments of this problem were carried out by Giordano[53], and the published numerical results could be found in Deiterding[54] by GCIB method and in Tian[55] by penalty IB method.

As shown in Fig.13, this problem is simulated in the domain of length $L = 400\,\text{mm}$ and height $H = 80\,\text{mm}$. The flexible panel of length $l_4 = 50\,\text{mm}$ and thickness $h_2 = 1\,\text{mm}$ is clamped into a forward-facing step of length $l_1 = 265\,\text{mm}$ and height $h_1 = 15\,\text{mm}$ with the distance $l_3 = 250\,\text{mm}$ to the right-hand side of computational domain. The initial position of the incident shock is located to the left of the step with the distance $l_2 = 15\,\text{mm}$.

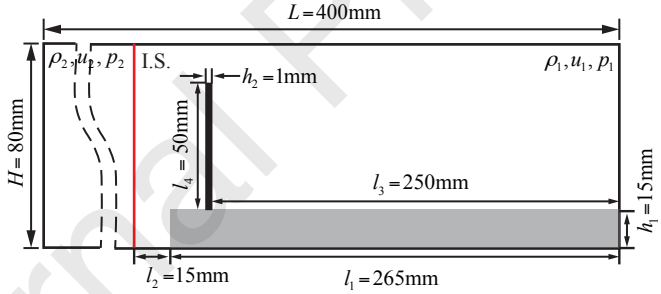

Figure 13: Diagram of computational domain for the shock-panel interaction simulation

The initial flow states ahead of I.S. are of density $\rho_1 = 1.2\,\text{kg/m}^3$, pressure $p_1 = 100\,\text{KPa}$, velocity $u_1 = 0\,\text{m/s}$ and $v_1 = 0\,\text{m/s}$, and those behind I.S. are of density $\rho_2 = 1.6548\,\text{kg/m}^3$, pressure $p_2 = 156.18\,\text{KPa}$, velocity $u_2 = 112.61\,\text{m/s}$ and $v_2 = 0\,\text{m/s}$. The fluid is of the ideal gas EOS with the parameter $\gamma = 1.4$. The material parameters for the flexible panel are density $\rho_s = 7.6 \times 10^3\,\text{kg/m}^3$, Young's modulus $E_s = 220\,\text{GPa}$ and Poisson's rate $\nu = 0$. And the forward-facing step is set as an approximately fixed rigid body with sufficient large density $\rho_\infty \sim 10^{14}\,\text{kg/m}^3$ and Young's modulus $E_\infty \sim 10^8\,\text{GPa}$.

The mesh size of the computational domain is 0.25 mm. The flexible panel is discretized into 3200 particles of the volume $0.125\,\text{mm} \times 0.125\,\text{mm}$, and the forward-facing step is discretized into 254400 particles with the same volume. The inlet boundary conditions are imposed on the left-hand side and rigid wall boundary conditions anywhere else.

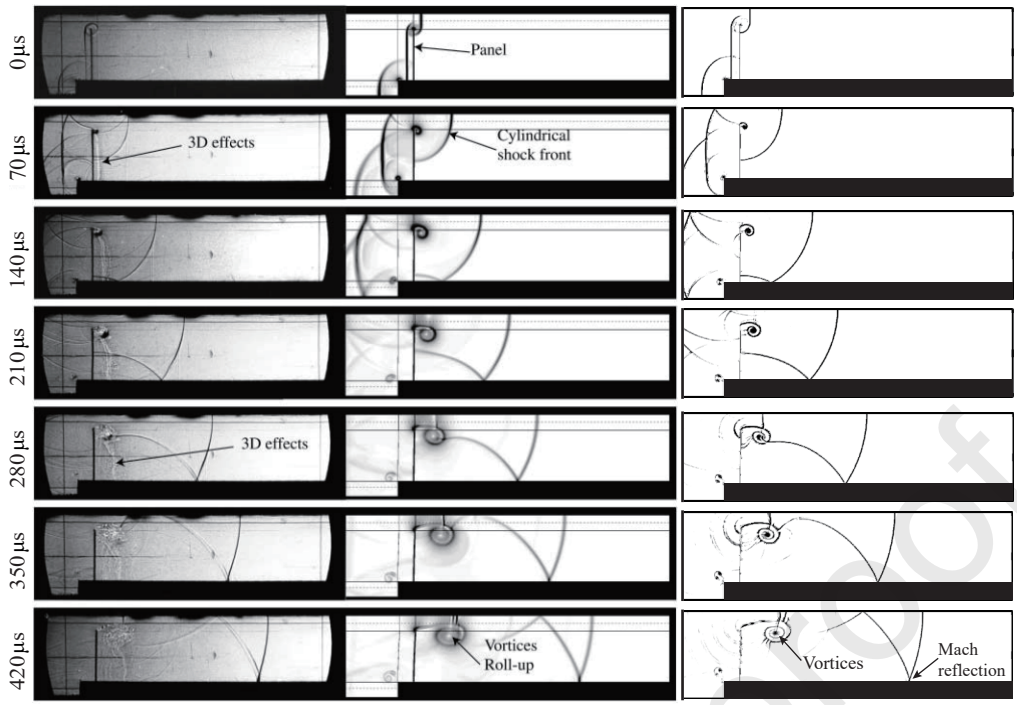

(a) Experiment and simulation data from Giordano(2005) (b) Shadowgraph of IBMPM

Figure 14: Numerical results of the shock-panel interaction simulation from 0 μs to 420 μs per 70 μs

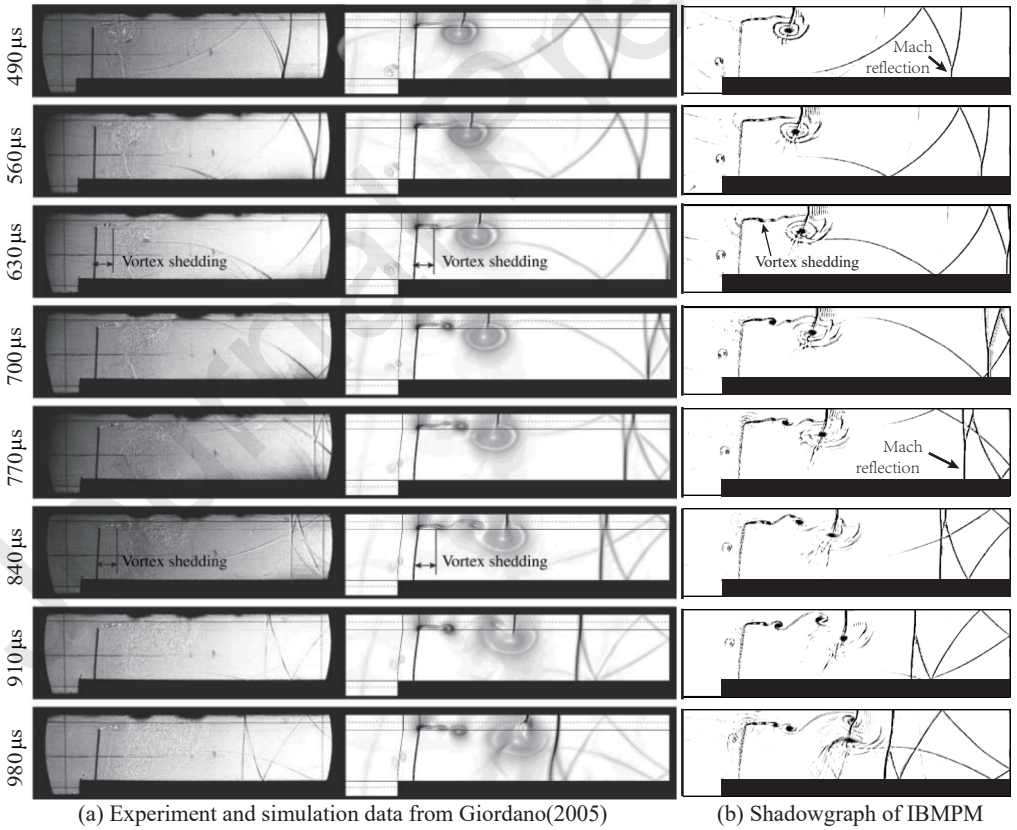

(a) Experiment and simulation data from Giordano(2005) (b) Shadowgraph of IBMPM

Figure 15: Numerical results of the shock-panel interaction simulation from 490 μs to 980 μs per 70 μs

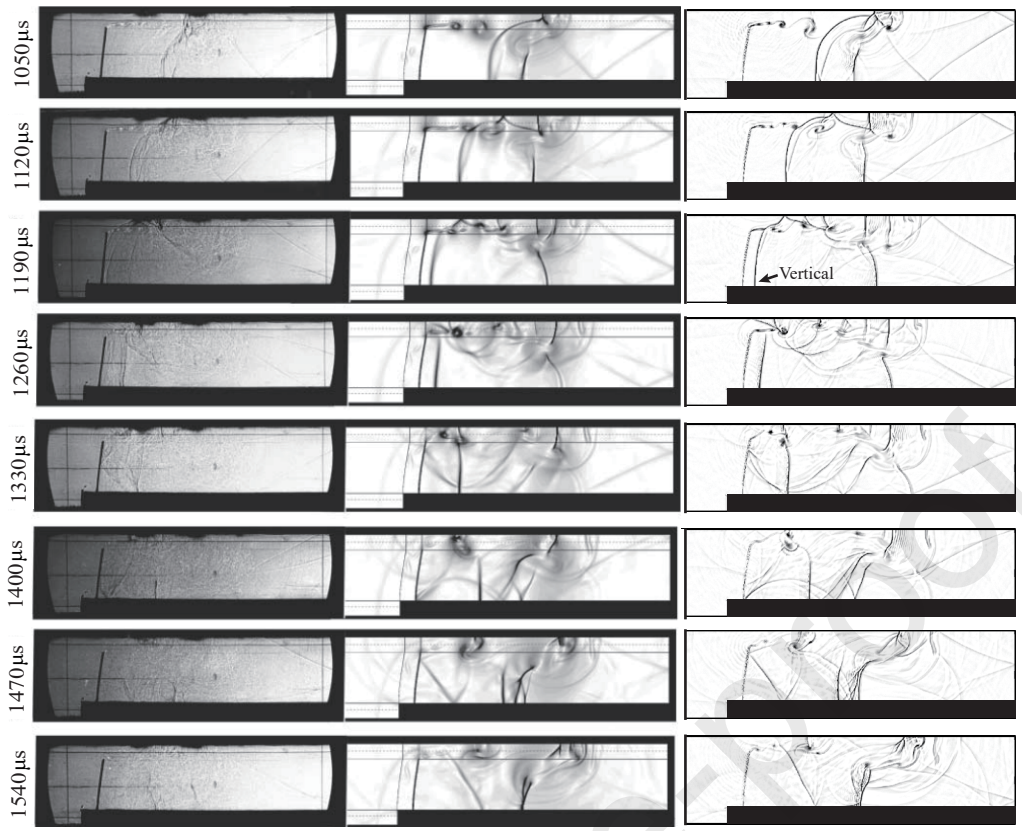

(a) Experiment and simulation data from Giordano(2005) (b) Shadowgraph of IBMPM

Figure 16: Numerical results of the shock-panel interaction simulation from 1050 μs to 1540 μs per 70 μs

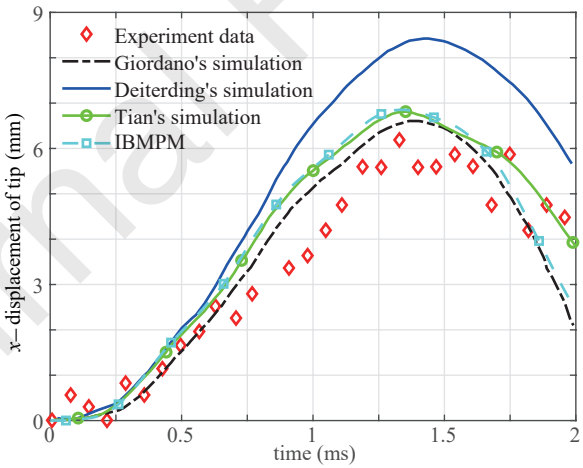

Figure 17: x-Displacement of the flexible panel top tip for 2 ms

The experiment shadowgraphs, numerical schlieren of Giordano[53] and the shadowgraphs of IBMPM from 0 μs to 1540 μs with the time interval 70 μs are depicted in Figs.14, 15 and 16. The origin of time $t = 0$ μs is defined the same as Giordano[53] at the instant when the incident shock wave interacts with the panel, reflected and transmitted shock waves appear. The numerical shadowgraphs of present simulation by IBMPM are in good agreement with those of Giordano[53]. The phenomena of reflected shock waves, vortex produced by the roll-up of the slipstream initiated from the panel ending, vortex shedding and vortex motion are all correctly reproduced. Especially, as illustrated in Fig.14 $t = 420$ μs, Fig.15 $t = 490$ μs and $t = 770$ μs, IBMPM reproduces the Mach reflection upon the top surface of the forward-facing step as well as Giordano[53].

The x-displacement of the flexible panel top tip versus time is plotted in Fig.17. Comparing with the numerical results in the literature, IBMPM gives a good fit for the experiment data in the time of peak value and the largest displacement, which verifies the imposition of the immersed boundary force conditions.

6.5. Fragmentation of a cylinder shell

Tang[56] carried out the experiments to study the dynamic fracture of the 1045 steel cylinder shells driven by detonation. Yang and Zhang[57] applied the MPM to simulate this problem, in which both the explosive and steel shell are discretized by particles. In present work, the IBMPM is applied to this problem, with the explosive and surrounding air discretized into finite volume elements and the steel shell discretized by particles. And the numerical results of pure MPM discretization under the same initial and boundary conditions are also provided here for comparison.

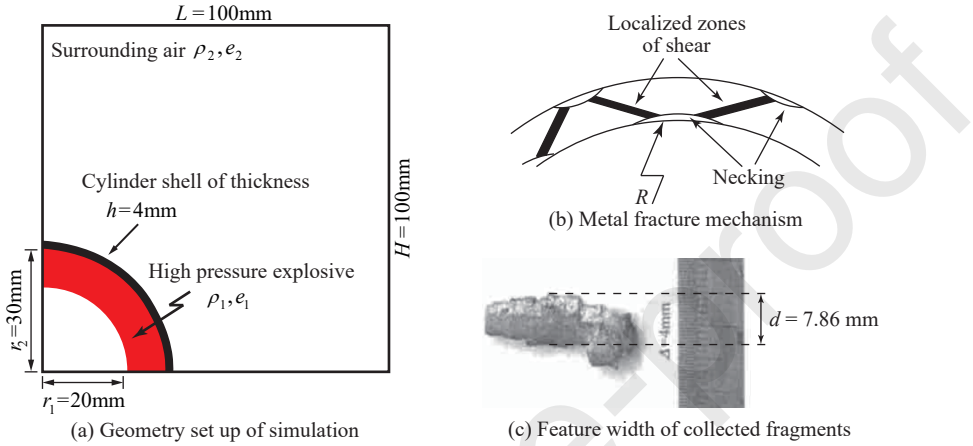

Figure 18: Simulation set-up and experiment results from Tang[56] of cylinder shell fragmentation driven by detonation

As shown in Fig.18(a), this problem is treated as a plain strain problem and a 1/4 model of the cylinder shell is simulated due to symmetry. The whole computational domain is of 100 mm × 100 mm × 0.5 mm and the mesh size is 0.5 mm in all the directions. The cylinder shell of inner radius $r_2 = 30$ mm and thickness $h = 4$ mm is discretized by particles of volume 0.25 mm × 0.25 mm × 0.25 mm. The boundary conditions at $x = 100$ mm and $y = 100$ mm are free boundaries for solid and outlet boundaries for fluid, while others are symmetric boundaries for solid and rigid wall boundaries for fluid. The explosive material used in Tang[56] is RHT-901 which has a density of $\rho = 1.684 \times 10^{-3}$ g/mm^3 and detonation energy per unit volume of $E_0 = 6853.9$ mJ/mm^3. And the surrounding air is of density $\rho_{\text{air}} = 1.2 \times 10^{-6}$ g/mm^3 and internal energy of $E_{\text{air}} = 0.25$ mJ/mm^3. The ideal gas EOS with the parameter $\gamma = 1.4$ is used for both the explosive and the surrounding air. The strength model of the solid steel is described by the simplified Johnson-Cook flow stress model as

$$\sigma_y = \left(A + B\bar{\varepsilon}_p^n\right)\left(1 + C\ln\dot{\varepsilon}_p^*\right) \tag{43}$$

where σ_y is the yield stress, A, B, n and C are material constants as listed in Table 1 from Chen[58], $\bar{\varepsilon}_p$ is the effective plastic strain and $\dot{\varepsilon}_p^* = \dot{\bar{\varepsilon}}_p/\dot{\varepsilon}_0$ is the dimensionless effective plastic strain rate. And the Mie-Gruneisen EOS with parameters $c_0 = 3570$ mm/ms, $s = 1.92$ and $\gamma_s = 1.8$ is used to update the volumetric stress for the solid steel.

Table 1: The constants of simplified Johnson-Cook model for 1045 steel

E(MPa)	A(MPa)	B(MPa)	C	n	ρ_s(g/mm^3)	ν
210000	507	320	0.064	0.28	0.0078	0.3

The effective plastic strain failure criterion with the Weibull random failure scheme is used to describe the failure behavior of the 1045 steel. The fracture strain ε_{f} of the cylinder shell is measured to be 0.43 in Tang[56], and thus the mean value of the effective strain in the Weibull random failure scheme is set to 0.43. And the two parameters of Weibull form are $\bar{\varepsilon}_0^p = 0.898$ and $m = 19.887$ as in Fok[59]. More details about the Johnson-Cook model for metal material and Weibull random failure scheme can be found in Appendix A.1.

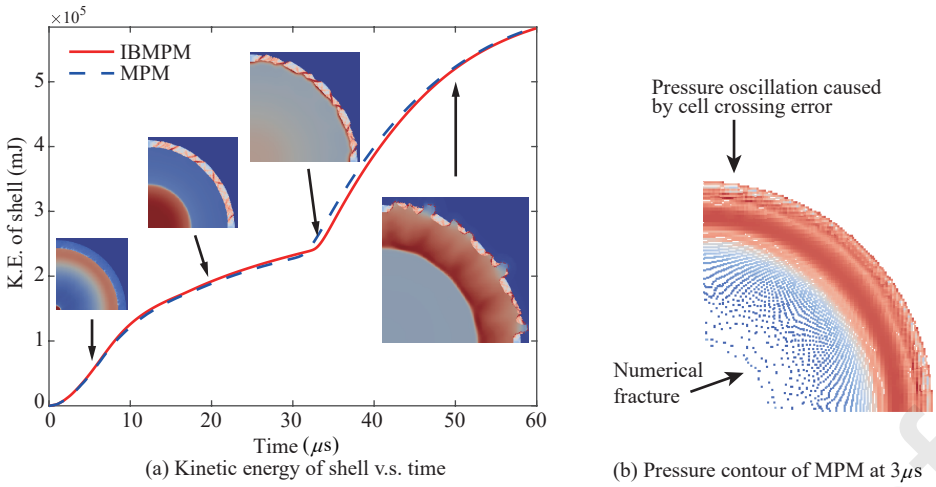

(a) Kinetic energy of shell v.s. time

(b) Pressure contour of MPM at 3μs

Figure 19: (a) Kinetic energy of the cylinder shell versus time. Four contours of pressure in fluid and effective plastic strain in solid are the results of IBMPM at time of 5μs, 20μs, 34μs and 50μs individually. (b) Pressure contour of MPM results at 3μs and numerical fracture.

The curve of cylinder shell kinetic energy versus time is depicted in Fig.19(a). At the beginning of simulation $t = 0\,\mu$s, an explosion wave and an implosion wave are generated, and the motion and dynamic fracture of the solid cylinder shell are driven by the explosion wave. At $t = 5\,\mu$s, the implosion wave reaches the origin (0 mm, 0 mm) and a reflection wave is generated. At around $t = 32\,\mu$s, the reflection wave catches up with the cylinder shell and drives the shell to accelerate which leads to the inflection point of the kinetic energy curve, and a secondary reflection wave with a slower moving speed M_S is generated. And from the instant of $t = 50\,\mu$s, the phenomena of pressure relief and gas leakage come to occur as shown in Figs.21(e) and 23(e).

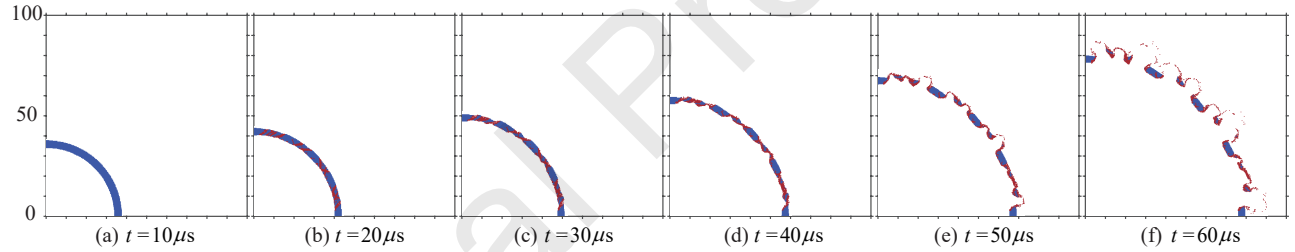

Figure 20: Numerical results of cylinder shell failure contour by IBMPM from 0μs to 60μs

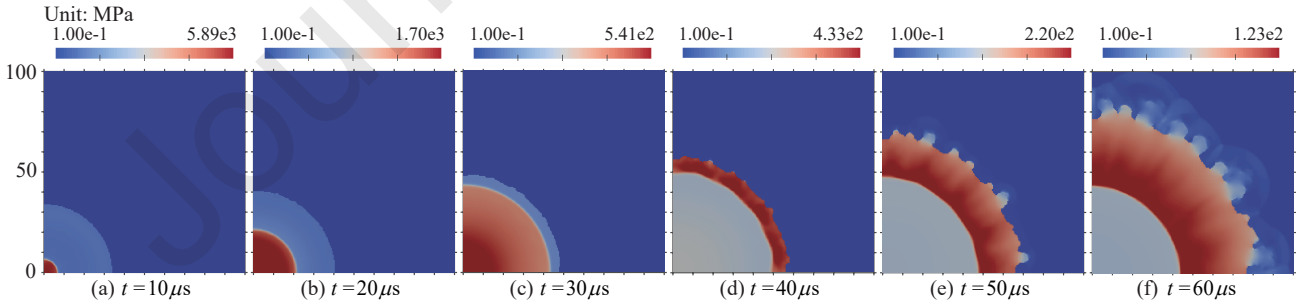

Figure 21: Pressure results of explosive and surrounding air by IBMPM from 0μs to 60μs

Numerical fracture will always occur when applying the MPM to the simulation of gas expansion as shown in Fig.19(b), and thus the shock wave surface cannot be maintained. If the surrounding air is also discretized by particles and simulated, material penetration and great non-physical oscillations will then occur at the shock wave surface, which leads to the simulation instability. Therefore, the surrounding air of 0.1 MPa is assumed to be vacuum compared with the high pressure explosive of several GPa in the simulation by pure MPM. In contrast,

IBMPM simulates the whole computational domain including the surrounding air and give a good representation for the shock wave surface as shown in the pressure contours in Fig.19(a) and Fig.21.

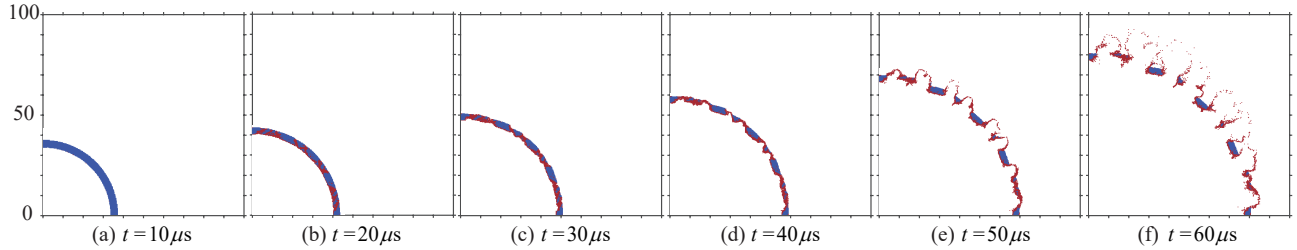

Figure 22: Numerical results of cylinder shell failure contour by MPM from 0μs to 60μs

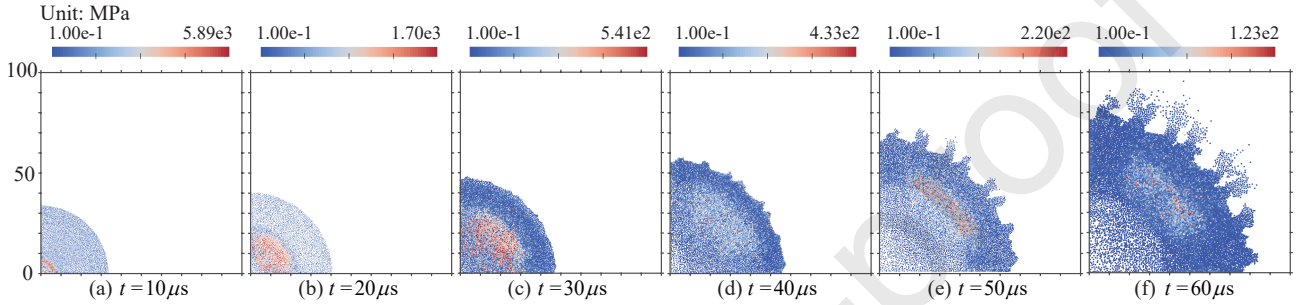

Figure 23: Pressure results of explosive by MPM from 0μs to 60μs

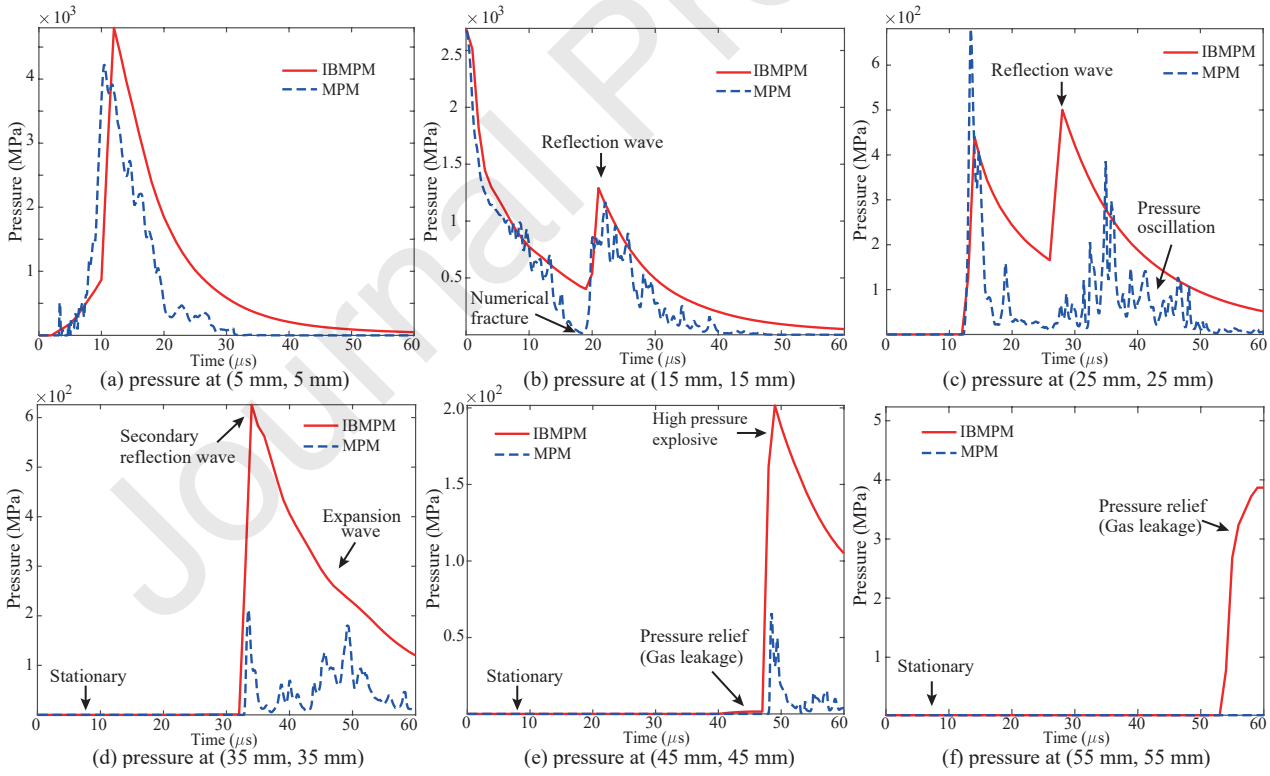

Figure 24: The pressure histories of fluid at different spatial points

The motions and dynamic fracture of the solid cylinder shell are depicted in Figs.20 and 22 where the red

particles are the particles at failure, while the pressure contours of explosive gas and surrounding air are depicted in Figs.21 and 23. The positions of fragments in IBMPM results and MPM results are almost the same. At the beginning of simulation, the pressure results of explosive gas in MPM are as good as that in IBMPM as shown in Fig.23(a) and (b). However, with time increasing, numerical fracture and great pressure oscillations come to occur due to the Lagrangian description of particle and cell-crossing noise. From the results of Fig.21(f) and Fig.23(f), we can find that the phenomenon of pressure relief in IBMPM is much intenser than that in MPM due to the better representation and maintenance of the shock wave surface.

The fluid pressure history curves at six spatial points of (5 mm, 5 mm), (15 mm, 15 mm), (25 mm, 25 mm), (35 mm, 35 mm), (45 mm, 45 mm) and (55 mm, 55 mm) are plotted in Fig.24. As illustrated in Fig.24, various pressure stages are well captured by IBMPM, namely stationary flow, implosion/explosion wave, reflection wave, secondary reflection wave, expansion wave and pressure-relief (also known as gas leakage) phenomenon. As shown in Fig.24(a) and (b), MPM gives a good result for pressure before $t = 10\,\mu$s, but great oscillations in pressure occur in the following time steps. And numerical fracture phenomenon in MPM is also observed by the sudden decrease in pressure at $t = 18\,\mu$s in Fig.24(b). Also, the pressure of secondary reflection wave and expansion wave in MPM is much lower than that of IBMPM due to the heavy pressure oscillation as shown in Fig.24(d) and (e). Because the surrounding air out of cylinder shell is not simulated in MPM, the pressure stages of pressure-relief phenomenon can not be captured by MPM as shown in Fig.24(f).

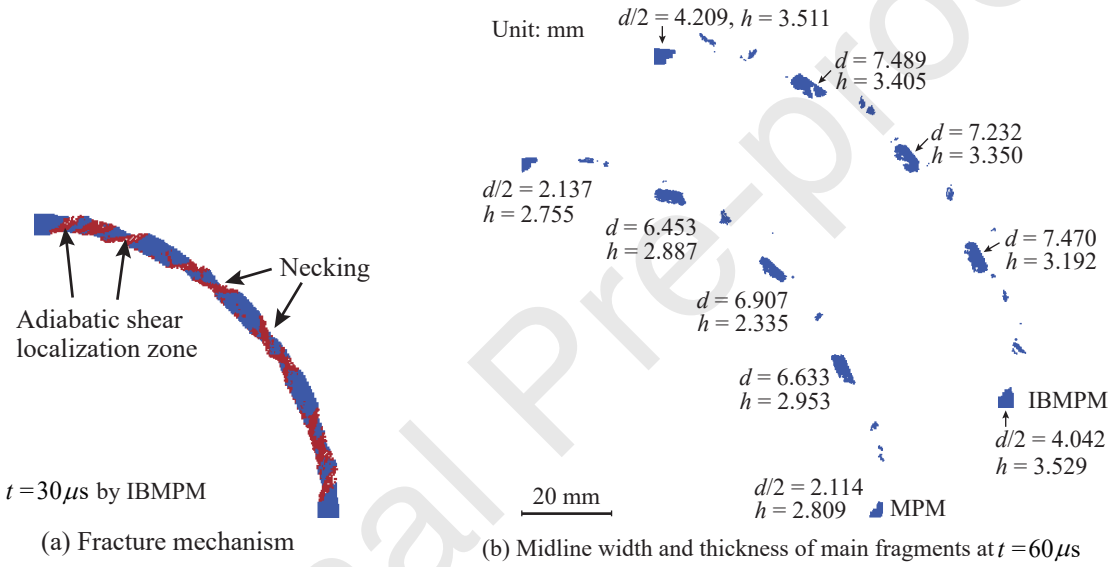

Figure 25: Fracture mechanism captured by IBMPM and the midline width of main fragments at the end of simulation

Table 2: Statistics of fragments' midline width and thickness at the end of simulation (Unit: mm)

Simulation method	Midline-width/Thickness of main fragments					Average width/thickness
MPM	4.274/2.755	6.453/2.887	6.907/2.335	6.633/2.953	4.228/2.809	5.699/2.748
IBMPM	8.418/3.511	7.489/3.405	7.232/3.350	7.470/3.192	8.084/3.529	7.739/3.397
Experiment [56]			/			7.86/3.3

As shown in Fig.18(b), the shear localization was risen by the high strain rate in detonation, resulting in the severe plastic deformation and necking of the shell. The fracture mechanism captured by IBMPM is also illustrated in Fig.25(a). Reviewing the whole process of fracture, the material points located at the inner side of the shell fail firstly. When the expanding proceeded, the adiabatic shear localization zones and necking phenomenon occur, which stem from the failed material points. At last, cracks are initiated along the shear band and lead to the heavy topology change as shown in Fig.20.

The midline width and thickness of main fragments at the end of simulation are measured as marked in Fig.25(b), and are summarized in the Table 2 together with the experiment results from Tang[56]. The pure MPM provides much smaller fragments, while the IBMPM gives satisfactory results both in midline width and thickness comparing with the experiment data. As common sense, there exists great difference between the compressibility of the explosive gas and the steel shell. However, the fluid-structure interaction in the pure MPM is implemented by the same velocity field for both the fluid domain and the solid structure. And, the velocity divergence, $\nabla \cdot \boldsymbol{v}$, measures the material compressibility. That is, the material points of the explosive gas and the steel shell near the FSI interface share the same compressibility, which leads to severer fracture and smaller fragments in MPM simulation. As evidence, all the material points located at the inner side of the shell have already failed at the very beginning of MPM simulation as shown in Fig.22(b).

6.6. Blast impact on the reinforced concrete slab

Wang[60] carried out the experiments to study the damage mode of a square reinforced concrete slab under close-in explosion as shown in Fig.26(a), and the reinforcement was arranged as illustrated in Fig.26(b) for 1/4 model. For the sake of symmetry, the 1/4 model of the reinforced concrete slab is simulated in the present work as shown in Fig.26(c). Both of the IBMPM and the pure MPM are applied to this problem to demonstrate the advantages of IBMPM over MPM.

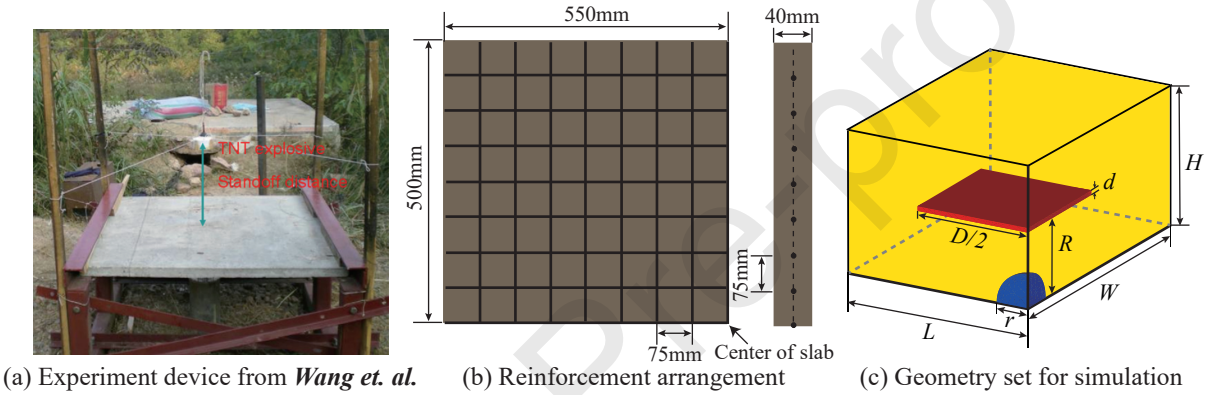

(a) Experiment device from ***Wang et. al.*** (b) Reinforcement arrangement (c) Geometry set for simulation

Figure 26: Geometry setup of experiments from Wang[60] and for simulations

The whole computational domain is of 600 mm × 600 mm × 600 mm, and the mesh size is 8 mm. The reinforced concrete slab of 550 mm × 500 mm × 40 mm is located at the standoff distance of $R = 400$ mm, and is discretized by particles of volume 2 mm × 2 mm × 2 mm. The spheric explosive charge is set at the origin of computational domain with the mass of $m = 0.46$ kg. For solid structure, the boundary conditions at $x = 0$ mm and $y = 0$ mm are symmetric boundaries, while others are free boundaries. For fluid domain, the boundary conditions at $x = 0$ mm, $y = 0$ mm and $z = 0$ mm are symmetric boundaries, while others are outlet boundaries. The explosive material used in Wang[60] is TNT which has a density of $\rho = 1.63 \times 10^{-3}\,\mathrm{g/mm^3}$ and detonation energy per unit volume of $E_0 = 7000\,\mathrm{mJ/mm^3}$. And the surrounding air is of density $\rho_{\mathrm{air}} = 1.2 \times 10^{-6}\,\mathrm{g/mm^3}$ and internal energy of $E_{\mathrm{air}} = 0.25\,\mathrm{mJ/mm^3}$. The ideal gas EOS with the parameter $\gamma = 1.4$ is used for both the explosive and the surrounding air. In the present work, the Holmquist-Johnson-Cook(HJC) dynamic damage model[61] is adopted for concrete. Specific description of the HJC model is listed in Appendix A.2, and the corresponding material constants from Wang[60] and Holmquist[61] are listed in Table 3 and Table 4. The Johnson-Cook model for steel 4340 is adopted for the reinforcement steel, and the material parameters from Wang[60] are: reference density, $\rho = 7.83\,\mathrm{g/cm^3}$; bulk modulus, $K = 159$ GPa; reference room temperature, $T_r = 300$ K; melting temperature, $T_m = 1793$ K; shear modulus, $G = 81.8$ GPa; basic yield stress, $A = 792$ MPa; hardening constant, $B = 510$ MPa; hardening exponent, $n = 0.26$; strain rate constant, $C = 0.014$; and thermal softening exponent, $m = 1.03$.

Table 3: The material constants of Holmquist-Johnson-Cook(HJC) strength model for concrete

A	B	N	C	$f_c^{'}$(MPa)	$S_{\max}$	G(MPa)	T(MPa)	D_1	D_2	$\varepsilon_f^{\min}$	ρ_s(g/mm^3)	ν
0.79	1.60	0.61	0.007	39.5	7.0	28	4.2	0.04	1.0	0.0008	0.00255	0.2

Table 4: The material constants of Holmquist-Johnson-Cook(HJC) EOS model for concrete

P_{crush}(MPa)	μ_{crush}	K_1(GPa)	K_2(GPa)	K_3(GPa)	P_{lock}(GPa)	μ_{lock}
16	0.001	85	-171	208	0.80	0.10

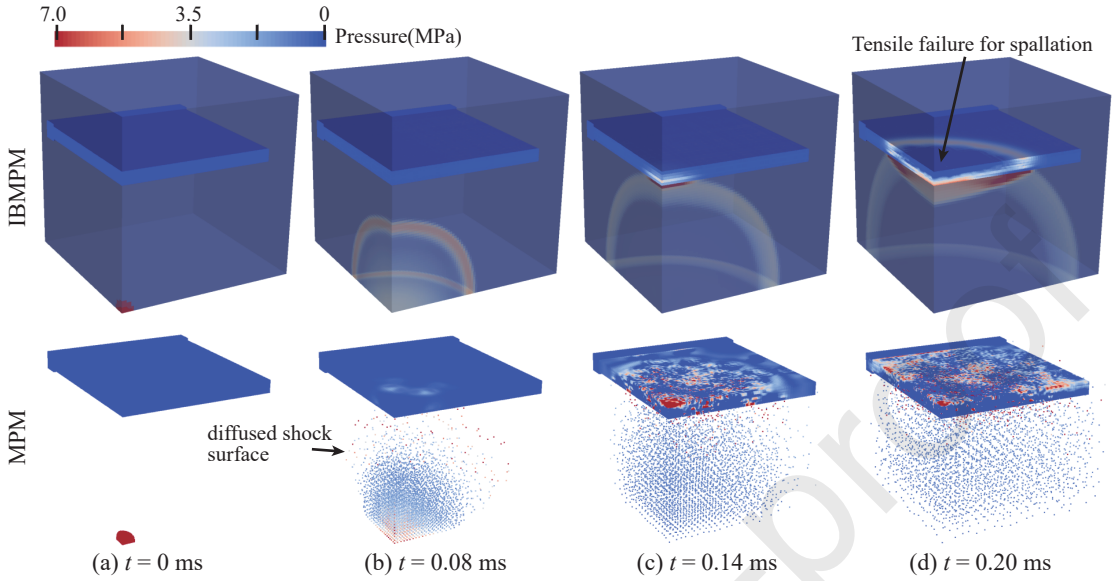

Figure 27: Pressure contour results of the IBMPM and the pure MPM

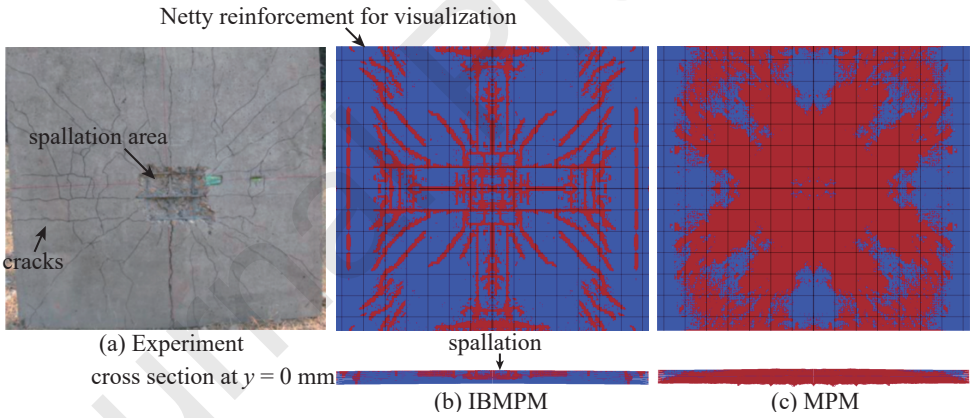

Figure 28: Damage modes of the reinforced concrete slab

The pressure contour results of explosive gas, surrounding air and reinforced concrete slab by IBMPM and MPM are depicted in Fig.27. Propagation and reflection of the explosive wave are well captured by the IBMPM, and the representation of the explosive wave front keeps sharp. And at $t = 0.20$ ms in IBMPM, there exists a tensile failure zone at the back of the slab which gives rise to the phenomenon of spallation. However in the pure MPM, the representation of the explosive wave front becomes diffused during simulation due to the cell-crossing noise and numerical fracture. Thus, the explosive wave has already interacted with the reinforced concrete slab at $t = 0.08$ ms in MPM, while not until $t = 0.14$ ms in IBMPM. In MPM, those material points representing the wave front are of high velocity and strike the reinforced concrete slab so hardly that bits and pieces of non-physical high pressure zones can be observed on the reinforced concrete.

The damage contour results simulated by IBMPM and MPM are depicted in Fig.28 and imply the damage modes on the reinforced concrete slab. And, the netty reinforcement depicted in black lines is artificially moved to the surface of the slab for visualization to locate the positions of cracks and spalling area. As shown in Fig.28(a),

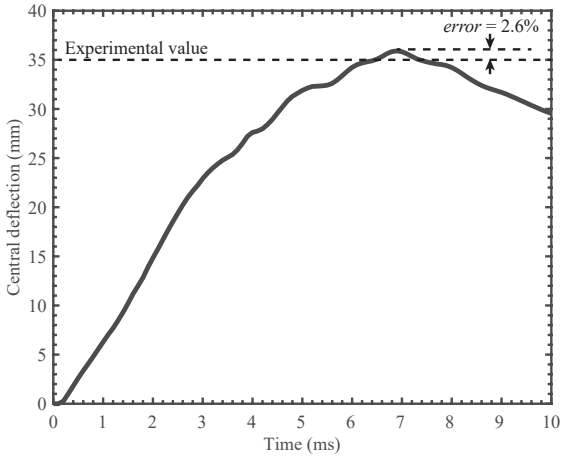

Figure 29: Central deflection of the reinforced concrete slab by IBMPM

the slab exhibited moderate damage and spalling occurred at the back surface of the slab. As for the size of spalling area, the radius reported in Wang[60] was approximately 120 mm and the thickness was about half of the slab's thickness due to the reinforcement taking the responsibility for tension. Also, there were respectively three horizontal and vertical cracks along the direction of the reinforcement steel, and there were various incline cracks at an approximate angle of 45°. As shown in Fig.28(b), the damage modes of cracks and spallation captured by the IBMPM are in good agreement with the experimental results. In the numerical simulation, the radius of the spalling area is 129 mm, slightly wider than the experimental result. And from the central cross section at $y = 0$ mm of IBMPM, we can find that the phenomenon of spallation also stops at the midline of the reinforced concrete slab. However in MPM, the whole slab is almost destroyed and the damage modes of cracks and spallation can not be observed as shown in Fig.28(c).

The central deflection curve of the reinforced concrete slab by IBMPM is plotted in Fig.29, while the pure MPM can not give out this curve due to the severe damage at the center of the slab. The largest deflection reported in Wang[60] was 35 mm as depicted in Fig.29. And, the largest deflection given by IBMPM simulation is 35.9 mm which is consistent with the experimental result considering the relative error of 2.6%.

6.7. Explosive impact on the expansion ring

In the experiments of Hiroe[62], ring specimens were placed onto a single cylinder filled with high explosive of powder pentaerythritol-tetranitrate(PETN) as a expansion driver. And, each ring specimen was seperated into about 20 fragments as shown in Fig.30(a). However, the charge density of PETN was not provided throughout his article. Thus, the IBMPM is applied for simualtions with different charge densities in the present work to find out the reasonable one.

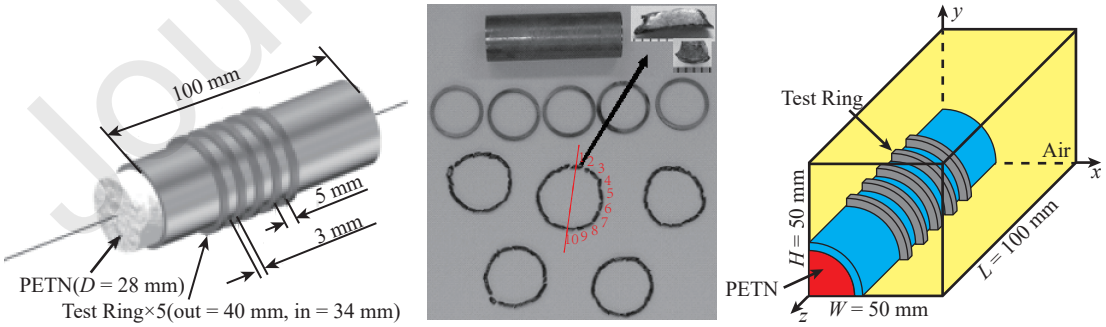

(a) Experimental set-up and fragment results from ***Hiroe et. al.*** (b) 1/4 model for simualtion

Figure 30: Setup of explosive impact on the expansion ring from Hiroe[62]

As shown in Fig.30(b), the 1/4 model is adopted for simulations due to symmetry. The whole computational domain is of $L = 100$ mm, $W = 50$ mm and $H = 50$ mm, and the mesh size is 0.4 mm. The cylinder driver of

inner radius $r_{c,in} = 14\,mm$, length $L_c = 100\,mm$ and thickness $h_c = 3\,mm$ is discretized by particles of volume $0.2\,mm \times 0.2\,mm \times 0.2\,mm$. The expansion rings of $r_{l,in} = 17\,mm$, length $L_l = 3\,mm$ and thickness $h_l = 3\,mm$ are placed at the same positions in experiment and discretized by particles of volume $0.2\,mm \times 0.2\,mm \times 0.2\,mm$. The boundary conditions at $x = 50\,mm$ and $y = 50\,mm$ are free boundaries for solid and outlet boundaries for fluid, while others are symmetric boundaries for solid and rigid wall boundaries for fluid. The high explosive of PETN from Li[63] has detonation energy per unit mass of $E_0 = 4.0635\,kJ/g$, and the charge density is chosen from Table 5. The strength model of 304 stainless steel(304SS or JIS SUS304) used in experiments is described by the simplified Johnson-Cook flow stress model and corresponding material parameters from Mousavi[64] are listed in Table 6. And the Mie-Gruneisen EOS with parameters $c_0 = 3570\,mm/ms$, $s = 1.92$ and $\gamma_s = 1.8$ is used to update the volumetric stress for the solid steel. The effective plastic strain failure criterion with the Weibull random failure scheme is used to describe the failure behavior of the 304SS steel. From the time-history curve of wall radii at the mid-length for expanding cylinders in Hiroe[62], we can calculate the fracture strain $\varepsilon_f = 0.4559$, and thus the mean value of the effective strain in the Weibull random failure scheme is set to 0.4559 with $\bar{\varepsilon}_0^p = 0.898$ and $m = 19.887$.

Table 5: The charge density list for simulation

Charge density ρ_{PETN} (g/cm^3)	0.86	0.96	1.06	1.16	1.26
Detonation velocity (m/s)	5326	5652	5979	6306	6633

Table 6: The constants of simplified Johnson-Cook model for 304SS steel

E(MPa)	A(MPa)	B(MPa)	C	n	ρ_s(g/cm^3)	ν
193000	792	510	0.014	0.26	8.03	0.26

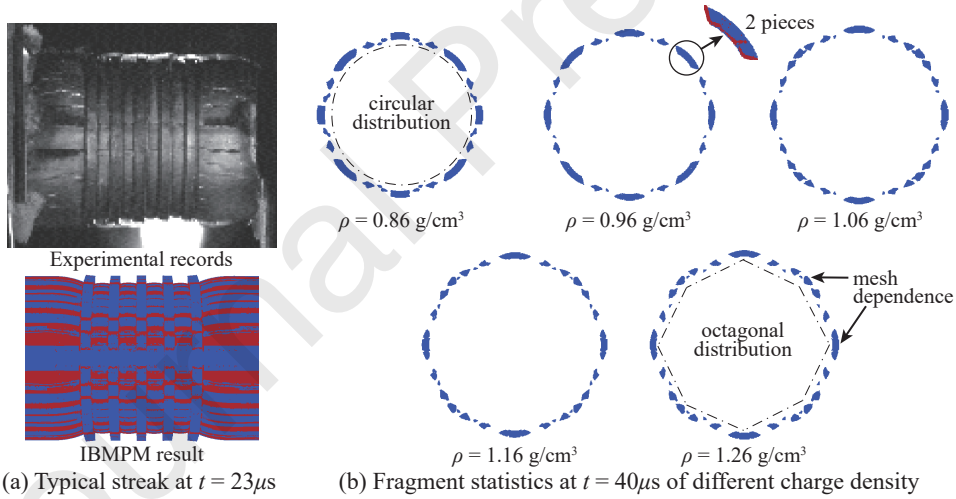

(a) Typical streak at $t = 23\mu s$ (b) Fragment statistics at $t = 40\mu s$ of different charge density

Figure 31: Simulation results for the expansion loop problem

Typical framing and streak at $t = 23\mu s$ are depicted in Fig.31(a), and fragments' shapes of different charge densities at $t = 40\mu s$ are plotted in Fig.31(b). With charge density increasing, the size of fragments becomes smaller, especially at the angle of $\theta = \pm 45^o, \pm 135^o$. In this sense, the simulation result of $\rho_{PETN} = 0.96\,g/cm^3$ provides the fragments' number of 20 pieces which is in the best agreement with experimental statistics. For simplicity, the IBMPM describes the cracks by the failed material points in the present work (details can be found in Appendix B), which however is of mesh dependence. Thus, fragments oblique to the structured mesh suffer much severer fracture than those distributed along the mesh at the angle of $\theta = 0, \pm 90^o, 180^o$. And, the phenomenon of pressure relief is much intenser around these inclined fragments which leads to smaller push forces back these fragments. As a result, the distribution of fragments transforms from circle at $\rho_{PETN} = 0.86\,g/cm^3$ gradually to octagon at $\rho_{PETN} = 1.26\,g/cm^3$ as shown in Fig.31(b).

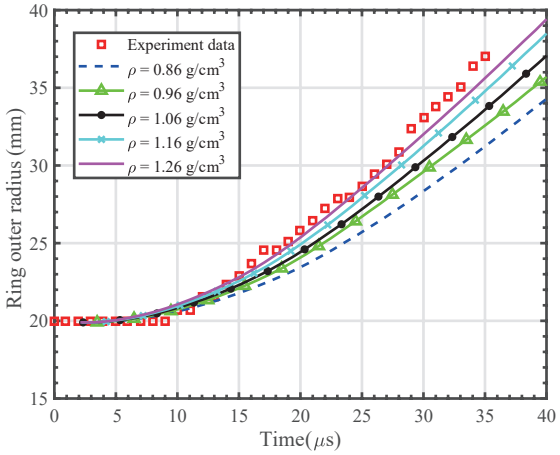

Figure 32: Time-histories of ring outer radius during expansion

The high explosive of PETN was detonated by the copper wire at the center of device in Hiroe[62] as shown in Fig.30(a), while the high explosive is assumed simultaneously detonated in our simulations. Thus, considering the different detonation velocities in Table 5, the time-histories of ring outer radius are plotted in Fig.32. It is obvious that the rings expand faster with the charge density increasing. And the simulation result of $\rho_{\mathrm{PETN}} = 1.26\,\mathrm{g/cm^3}$ gives the best fit for the experimental data.

In conclusion, considering the shortcomings of mesh dependence in crack description, $\rho_{\mathrm{PETN}} = 1.26\,\mathrm{g/cm^3}$ is the reasonable value for the charge density of PETN used in Hiroe[62].

7. Conclusions

A novel immersed boundary-material point method (IBMPM) is proposed in the present work for the simultaneous simulations of shock-structure interaction and accompanied dynamic fracture. This method consists of three parts, namely Riemann solver for fluid flow, MPM solver for solid structure and a novel Lagrangian continuous-forcing immersed boundary method (lg-CFIBM) with two schemes for the fluid-solid interaction. By combining the concepts of traditional penalty IBM and GCIB method, thelg-CFIBM is implemented in the frame of continuous force IBM with a compact support area for the immersed boundary conditions. It can guarantee the boundary velocity conditions strictly at each time step and has no need to reconstruct FSI interfaces, which makes it a promising method for the simultaneous simulations of shock-structure interaction and accompanied dynamic fracture.

We carry out two analytical cases of 1D string vibration problem and 2D vortex evolution problem to verify the convergence rates of MPM solver and Riemann solver individually. And then two benchmark cases of shock-cylinder obstacle interaction and flexible panel deformation induced by shock wave are conducted to validate the IBMPM. Numerical results are in great agreement with the published experiment data and numerical data by other FSI methods, which validates the imposition of the velocity and force boundary conditions. Finally, we apply the IBMPM to simulate the fragmentation of cylinder shell induced by explosive detonation, blast impact on the reinforced concrete slab and explosive impact on the expansion ring. All the results of IBMPM are in good agreement with the corresponding experiments and illustrate the advantages of IBMPM over MPM in the FSI simulations.

The Riemann solver is implemented with a uniform mesh in single-phase fluid flow in the present work. When applying to the explosive problems, the material model for the explosive production is set the same ideal gas equation of state as the surrounding air, which however should be JWL equation of state as in the experiments. The multi-phase Riemann solver will be implemented in future work. Also, an adaptive mesh refinement will be taken into consideration to accelerate the simulation speed. Besides, a more accurate description of cracks will be introduced to overcome the shortcomings of mesh dependence in future work.

References

[1] C.S. Peskin. Numerical analysis of blood flow in the heart. *Journal of Computational Physics*, 25:220–252, 1977.

[2] R. Mittal and G. Iaccarino. Immersed boundary methods. *Annual Review of Fluid Mechanics*, 37(1):239–261, 2005.

[3] S.E. Hieber and P. Koumoutsakos. An immersed boundary method for smoothed particle hydrodynamics of self propelled swimmers. *Journal of Computational Physics*, 227(19):8636–8654, 2008.

[4] W.-X. Huang, S.J. Shin, and H.J. Sung. Simulation of flexible filaments in a uniform flow by the immersed boundary method. *Journal of Computational Physics*, 226(2):2206–2228, 2007.

[5] W.-X. Huang. Improvement of mass source/sink for an immersed boundary method. *International Journal for Numerical Methods in Fluids*, 53:1659–1671, 2007.

[6] W.-X. Huang, C.B. Chang, and H.J. Sung. An improved penalty immersed boundary method for fluid flexible body interaction. *Journal of Computational Physics*, 230(12):5061–5079, 2011.

[7] A.M.A. Nasar, B.D. Rogers, A. Revell, P.K. Stansby, and S.J. Lind. Eulerian weakly compressible smoothed particle hydrodynamics (SPH) with the immersed boundary method for thin slender bodies. *Journal of Fluids and Structures*, 84:263–282, 2019.

[8] M. Hashemi, R. Fatehi, and M. Manzari. Simulating fluid solid interaction problems using an immersed boundary SPH method. 2011.

[9] S. Wang, G. Zhang, Y. Cai, B. Yan, and Q. Tang. Comparisons of two representative methods classified as immersed boundary and domain methods. *Engineering Analysis with Boundary Elements*, 132:383–398, 2021.

[10] T. Ye, N. Phan-Thien, C.T. Lim, L. Peng, and H. Shi. Hybrid smoothed dissipative particle dynamics and immersed boundary method for simulation of red blood cells in flows. *Phys Rev E.*, 95:063314, 2017.

[11] S.E. Vasilakis, C. Rodriguez, N. Kyriazis, I. Malgarinos, P. Koukouvinis, and M. Gavaises. A direct forcing immersed boundary method for cavitating flows. *International Journal for Numerical Methods in Fluids*, 93:3092–3130, 2021.

[12] I. Lee and H. Choi. A discrete-forcing immersed boundary method for the fluid-structure interaction of an elastic slender body. *Journal of Computational Physics*, 280:529–546, 2015.

[13] J. Wang and C. Zhou. A novel immersed boundary method implemented by imposing reconstructed velocity on virtual boundary. *Advances in Applied Mathematics and Mechanics*, 13(1):83–100, 2020.

[14] I. Borazjani, L. Ge, and F. Sotiropoulos. Curvilinear immersed boundary method for simulating fluid structure interaction with complex 3d rigid bodies. *Journal of Computational Physics*, 227(16):7587–7620, 2008.

[15] L. Ge and F. Sotiropoulos. A numerical method for solving the 3d unsteady incompressible navier-stokes equations in curvilinear domains with complex immersed boundaries. *Journal of Computational Physics*, 225(2):1782–1809, 2007.

[16] A. Gilmanov and F. Sotiropoulos. A hybrid cartesian/immersed boundary method for simulating flows with 3d, geometrically complex, moving bodies. *Journal of Computational Physics*, 207(2):457–492, 2005.

[17] A. Gilmanov and S. Acharya. A hybrid immersed boundary and material point method for simulating 3d fluid structure interaction problems. *International Journal for Numerical Methods in Fluids*, 56:2151 – 2177, 04 2008.

[18] H. Yoon and S. Shin. Simulation of sloshing in a bi-lobe tank under arbitrary rotation using the fds scheme and the hcib method. *Journal of Mechanical Science and Technology*, 26:3491–3501, 11 2013.

[19] D. Clarke, M. Salas, and H. Hassan. Euler calculations for multi-element airfoils using cartesian grids. *AIAA Journal*, 24:1128–35, 1986.

[20] H.S. Udaykumar, W. Shyy, and M.M. Rao. Elafint: A mixed eulerian-lagrangian method for fluid flows with complex and moving boundaries. *International Journal for Numerical Methods in Fluids*, 22:691–712, 1996.

[21] C. Brehm and H.F. Fasel. A novel concept for the design of immersed interface methods. *Journal of Computational Physics*, 242:234–267, 2013.

[22] A. Chaudhuri, A. Hadjadj, and A. Chinnayya. On the use of immersed boundary methods for shock/obstacle interactions. *Journal of Computational Physics*, 230(5):1731–1748, 2011.

[23] J. Boustani, M.F. Barad, C.C. Kiris, and C. Brehm. Fully-coupled fluid-structure interaction simulations of a supersonic parachute. 2019.

[24] F.H. Harlow and M.W. Evans. A machine calculation method for hydrodynamic problems. *LAMS-1956*, 1955.

[25] F.H. Harlow. The particle-in-cell computing method for fluid dynamics. *Methods Comput. Phys.*, 3:319–343, 1964.

[26] J.U. Brackbill and H.M. Ruppel. FLIP: A method for adaptively zoned, particle-in-cell calculations of fluid flows in two dimensions. *Journal of Computational Physics*, 65(2):314 – 343, 1986.

[27] J.U. Brackbill, D.B. Kothe, and H.M. Ruppel. FLIP: A low-dissipation, particle–in–cell method for fluid flow. *Computer Physics Communications*, 48(1):25 – 38, 1988.

[28] D. Sulsky, Z. Chen, and H.L. Schreyer. A particle method for history-dependent materials. *Comput. Methods Appl. Mech. Eng.*, 118:179–186, 1994.

[29] X. Zhang, Z. Chen, and Y. Liu. *The material point method: a continuum-based particle method for extreme loading cases*. Academic Press, 2016.

[30] W. Gong, Y. Liu, X. Zhang, and H. Ma. Numerical investigation on dynamical response of aluminum foam subject to hypervelocity impact with material point method. *Computer Modeling in Engineering & Sciences(CMES)*, 83(5):527–545, 2012.

[31] Y. Liu, H.K. Wang, and X. Zhang. A multiscale framework for high-velocity impact process with combined material point method and molecular dynamics. *Int. J. Mech. Mater. Des.*, 9(2):127–139, 2013.

[32] P. Huang, X. Zhang, S. Ma, and H. Wang. Shared memory openmp parallelization of explicit mpm and its application to hypervelocity impact. *CMES - Comput. Model. Eng. Sci.*, 38(2):119–148, 2008.

[33] S. Ma, X. Zhang, and X. Qiu. Comparison study of MPM and SPH in modeling hypervelocity impact problems. *Int. J. Impact Eng.*, 36(2):272–282, 2009.

[34] P. Huang, X. Zhang, S. Ma, and X. Huang. Contact algorithms for the material point method in impact and penetration simulation. *Internat. J. Numer. Methods Engrg.*, 85(4):498–517, 2011.

[35] Z. Ma, X. Zhang, and P. Huang. An object-oriented mpm framework for simulation of large deformation and contact of numerous grains. *CMES - Comput. Model. Eng. Sci.*, 55(1), 2010.

[36] Y. Liang, T. Benedek, X. Zhang, and Y. Liu. Material point method with enriched shape function for crack problems. *Comput. Methods Appl. Mech. Engrg.*, 322:541–562, 2017.

[37] P. Yang, Y. Liu, X. Zhang, X. Zhou, and Y. Zhao. Simulation of fragmentation with material point method based on gurson model and random failure. *CMES: Computer Modeling in Engineering & Sciences*, 85:207–236, 2012.

[38] F. Zhang, X. Zhang, K.Y. Sze, Y. Lian, and Y. Liu. Incompressible material point method for free surface flow. *J. Comput. Phys.*, 330:92–110, 2017.

[39] Y. Song, Y. Liu, and X. Zhang. A transport point method for complex flow problems with free surface. *Computational Particle Mechanics*, 7:377–391, 2020.

[40] X. Zhao, D. Liang, and M. Martinelli. Numerical simulations of dam-break floods with mpm. *Procedia Engineering*, 175:133–140, 2017.

[41] A.R. York, D. Sulsky, and H.L. Schreyer. Fluid-membrane interaction based on the material point method. *Internat. J. Numer. Methods Engrg.*, 48(6):901–924, 2000.

[42] J.G. Li, Y. Hamamoto, Y. Liu, and X. Zhang. Sloshing impact simulation with material point method and its experimental validations. *Comput. and Fluids*, 103:86–99, 2014.

[43] D. Liang, X. Zhao, and M. Martinelli. Mpm simulations of the interaction between water jet and soil bed. *Procedia Engineering*, 175:242–249, 2017.

[44] M. Martinelli, A. Rohe, and K. Soga. Modeling dike failure using the material point method. *Procedia Engineering*, 175:341–348, 12 2017.

[45] E. Fern, A. Rohe, K. Soga, and E. Alonso. *The Material Point Method for Geotechnical Engineering: A Practical Guide*. CRC Press, 01 2019.

[46] S. Ma, X. Zhang, Y. Lian, and X. Zhou. Simulation of high explosive explosion using adaptivematerial point method. *CMES: Computer Modeling in Engineering & Sciences*, 39:101–123, 2009.

[47] R. Ni and X. Zhang. A precise critical time step formula for the explicit material point method. *International Journal for Numerical Methods in Engineering*, 121:4989–5016, 2020.

[48] S.G. Bardenhagen. Energy conservation error in the material point method. *Journal of Computational Physics*, 180:383–403, 2002.

[49] V. Venkatakrishnan. On the accuracy of limiters and convergence to steady-state solutions. *AIAA paper 93-0880*, 1993.

[50] V.A. Titarev and E.F. Toro. Finite-volume weno schemes for three-dimensional conservation laws. *Journal of Computational Physics*, 201:238 – 260, 2004.

[51] J.Y. Yang, Y. Liu, and H. Lomax. Computation of shock wave reflection by circular cylinders. *AIAA Journal*, 25:683 – 689, 1987.

[52] A. E. Bryson and R. w. F. Gross. Diffraction of strong shocks by cones, cylinders, and spheres. *Journal of Fluid Mechanics*, 10:1 – 16, 1961.

[53] J. Giordano, G. Jourdan, Y. Burtschell, M. Medale, D. Zeitoun, and L. Houas. Shock wave impacts on deforming panel, an application of fluid-structure interaction. *Shock Waves*, 14:103–110, 2005.

[54] R. Deiterding, F. Cirak, and S.P. Mauch. Efficient fluid-structure interaction simulation of viscoplastic and fracturing thin-shells subjected to underwater shock loading. *Theory, Numerics and Applications*, pages 283–294, 2008.

[55] L. Wang, G.M.D. Currao, F. Han, A.J. Neely, J. Young, and F.-B. Tian. An immersed boundary method for fluid-structure interaction with compressible multiphase flows. *Journal of Computational Physics*, 346:131–151, 2017.

[56] T. G. Tang, Y. Gu, Q. Z. Li, J. S. Hua, and X. L. Sun. Expanding fracture of steel cylinder shell by detonation driving. *Explosion and Shock Waves*, 23:529–533, 2003.

[57] P. Yang, Y. Liu, X. Zhang, Y. Zhao, and X. Zhou. Simulation of fragmentation with material point method based on gurson model and random failure. *CMES: Computer Modeling in Engineering & Sciences*, 85:207–236, 2012.

[58] G. Chen, Z.F. Chen, W.F. Xu, Chen Y.M., and Huang X.C. Investigation on the j-c ductile fracture parameters of 45 steel. *Explosion and Shock Waves*, 27:131–135, 2007.

[59] S. Fok, B. Mitchell, and J. Smart. A numerical study on the application of the weibull theory to brittle materials. *Engineering Fracture Mechanics*, 68:1171–1179, 2001.

[60] Wei Wang, Duo Zhang, Fangyun Lu, Song chuan Wang, and Fujing Tang. Experimental study and numerical simulation of the damage mode of a square reinforced concrete slab under close-in explosion. *Engineering Failure Analysis*, 27:41–51, 2013.

[61] T.J. Holmquist, G.R. Johnson, and W.H. Cook. A computational constitutive model for concrete subjected to large strains, high strain rates, and high pressures. 1993.

[62] Tetsuyuki Hiroe, Kazuhito Fujiwara, Hidehiro Hata, Mitsuru Yamauchi, Kiyotaka Tsutsumi, and Takuya Igawa. Explosively driven expansion and fragmentation behavior for cylinders, spheres and rings of 304 stainless steel. *Materials Science Forum*, pages 1035–1040, 2010.

[63] LI Baohua, CHANG Bo, ZHANG Lijian, LYU Yongzhu, and GU Hongping. Influence of charge density on jwl equation of state of explosives. *Journal of Ordnance Equipment Engineering*, 42:174–178, 2021.

[64] S. A. A. Akbari Mousavi and A. Rahbar Kelishami. Experimental and numerical studies of the effects of process parameters in the continuous friction welding process. *Materials Science Forum*, pages 335–338, 2008.

[65] G.R. Johnson and W.H. Cook. A constitutive model and data for metals subjected to large strains, high strain rates, and high temperatures. pages 541–547, 1983.

[66] G.R. Johnson and T.J. Holmquist. Evaluation of cylinder-impact test data for constitutive model constants. *Journal of Applied Physics*, 64:3901–3910, 1988.

[67] M.A. Meyers. *Dynamic Behavior of Materials*. John Wiley & Sons, New York, 1994.

[68] A.S. Jayatilaka. *Fracture of engineering brittle materials*. Applied Science Publishers, 1979.

[69] H. Tadashi. Theory of failure of concrete and similar brittle solid on the basis of strain. *International Journal of Fracture Mechanics*, 5:73–79, 1969.

[70] J.A. Nairn. Material point method calculations with explicit cracks. *CMES: Computer Modeling in Engineering & Sciences*, 4:649–663, 2003.

Appendix A. Constitutive model

Constitutive models can be divided into strength models which relate the deviatoric stress to deviatoric strain, and equations of state(EOS) which relate the pressure to volume and internal energy or temperature. In addition, a failure criterion is required to identify the onset and describe the evolution of material failure.

Appendix A.1. Johnson–Cook constitutive model for metals

Appendix A.1.1. Johnson–Cook strength model

For explosion problems, Johnson and Cook [65,66] proposed a flow stress model to account for the strain hardening, strain rate, and thermal softening effects as follows:

$$\sigma_y = (A + B\varepsilon_p^n)(1 + C\ln\dot{\varepsilon}_p^*)(1 + T^{*m}) \tag{A.1}$$

where A, B, n, C and m are material constants, $\varepsilon_p = \sqrt{\frac{2}{3}\varepsilon_{ij}^{'}\varepsilon_{ij}^{'}}$ is the effective plastic strain,$\dot{\varepsilon}_p^* = \dot{\varepsilon}_p/\dot{\varepsilon}_0$ denotes the dimensionless effective plastic strain rate, $\dot{\varepsilon}_p$ represents the effective plastic strain rate, and $\dot{\varepsilon}_0 = 1.0\mathrm{s}^{-1}$ is the effective plastic strain rate corresponding to the quasi-static test used to determine the yield and hardening parameters A, B and n. $T^* = (T - T_r)/(T_m - T_r) \in [0, 1]$ denotes the dimensionless temperature, T is the temperature, T_r and T_m are the room temperature and melting temperature of the material.

Simplified Johnson–Cook flow stress model ignores the influence of temperature, i.e.

$$\sigma_y = (A + B\varepsilon_p^n)(1 + C\ln\dot{\varepsilon}_p^*) \tag{A.2}$$

Appendix A.1.2. Mie-Gruneisen EOS

The Mie–Gruneisen EOS [67] used to determine the pressure in a shock-compressed solid is given as

$$p = p_H + \frac{\gamma}{\nu}(e - e_H) \tag{A.3}$$

where p_H and e_H represent the pressure and specific internal energy on the Hugoniot curve, respectively, $\nu = 1/\rho$ is the specific volume, ρ is density, e is specific internal energy, and γ is the Gruneisen parameter determined by

$$\frac{\gamma}{\nu} = \frac{\gamma_0}{\nu_0} = \text{constant} \tag{A.4}$$

where γ_0 and ν_0 are the Gruneisen parameter and specific volume at the reference state, respectively. Substituting $p_H = p_0 + \frac{c_0^2(\nu_0-\nu)}{[\nu_0-s(\nu_0-\nu)]}$ and $e_H = e_0 + \frac{1}{2}(p+p_0)(\nu_0-\nu)$ into Eq.(A.3) and assuming $p_0 = 0$ and $e_0 = 0$ at the reference state, we have

$$p = p_H(1 - \frac{\gamma\mu}{2}) + \gamma_0 E \tag{A.5}$$

where c_0 denotes the bulk sound velocity at ambient pressure, s is a material constant, $\mu = \rho/\rho_0 - 1 = \nu_0/\nu - 1$, $E = \rho_0 e$, and ρ_0 is the density at the reference state.

For expanded materials, i.e., $\mu < 0$, the pressure is defined by

$$p = \rho_0 c_0^2 \mu + \gamma_0 E \tag{A.6}$$

Appendix A.1.3. Effective plastic strain failure criterion

In effective plastic strain failure scheme, a particle is assumed to be failed if its effective plastic strain ε^p exceeds a user-defined critical value $\varepsilon^p_{\max}$, i.e., $\varepsilon^p > \varepsilon^p_{\max}$.

On the basis of effective plastic strain failure scheme, Weibull statistical model is employed to describe the random characterization of fragmentation [68]. The Weibull theory for a uniaxial stress state can be written as

$$P_{\mathrm{f}} = 1 - \exp \int \left[-\left(\frac{\sigma - \sigma_{\mathrm{th}}}{\sigma_0} \right)^m \right] \frac{\mathrm{d}A}{a} \tag{A.7}$$

where P_{f} denotes the probability of failure, A represents the surface area and a is a unit area which is introduced for the consistency of units. $\sigma_0, \sigma_{\mathrm{th}}, m$ are respectively the mean strength, the threshold stress below which the material will not fail and a measure of scatter in the failure strengths of nominally identical components.

Eq.(A.7) is the three-parameter Weibull theory. If $\sigma_{\mathrm{th}} = 0$, the distribution becomes the two-parameter Weibull distribution as

$$P_{\mathrm{f}} = 1 - \exp \int \left[-\left(\frac{\sigma}{\sigma_0} \right)^m \right] \frac{\mathrm{d}A}{a} \tag{A.8}$$

Typically, the two-parameter Weibull distribution is used, and Fok [59] pointed out that the results for both two- and three-parameter predictions are similar when A = 1000. So the value A = 1000 will be used throughout the paper. The Weibull statistical theory in terms of strain was also investigated by Tadashi [69] who proved that the failure behavior of brittle solid can also be explained in terms of the stochastic process theory on the basis of strain. Therefore Eq.(A.8) takes the strain form as

$$P_{\mathrm{f}} = 1 - \exp \int \left[-\left(\frac{\varepsilon^p}{\varepsilon^p_0} \right)^m \right] \frac{\mathrm{d}A}{a} \tag{A.9}$$

where ε^p_0 is the mean strain.

Appendix A.2. Holmquist Johnson-Cook(HJC) constitutive model of concrete

A representative of concrete constitutive models is HJC model proposed by Holmquist and Johnson [61].

Appendix A.2.1. HJC strength model

The HJC model was originally presented for dynamic problems. In order to involve high strain rates and damage effects, the yield strength is expressed as

$$\sigma_y^* = (A(1-D) + Bp^{*n})(1 + C\ln\dot{\varepsilon}^*) \tag{A.10}$$

where $\sigma_y^* = \sigma_y/f_c^{'}$ denotes the normalized yield stress, σ_y is the actual yield stress, $f_c^{'}$ represents the quasi-static uniaxial compressive strength. $p^* = p/f_c^{'}$ denotes the normalized pressure, p the actual pressure. $\dot{\varepsilon}^* = \dot{\varepsilon}/\dot{\varepsilon}_0$ represents the dimensionless strain rate, $\dot{\varepsilon}$ the actual strain rate, $\dot{\varepsilon}_0 = 1.0\mathrm{s}^{-1}$ the reference strain rate. A, B, n, C and $S_{\max}$ are normalized cohesive strength, normalized pressure hardening coefficient, pressure hardening exponent, strain rate coefficient and normalized maximum strength, respectively.

Appendix A.2.2. HJC EOS

Considering high pressures and air voids, the EOS in HJC model is divided into three response regions including linear elastic zone, transition zone and full dense zone.

(1) Linear elastic zone

This zone arises at $p \leq p_{\text{crush}}$, where the material is at elastic state. Within this region, the EOS is given by

$$p = K_{\text{elastic}}\mu, \quad p \leq p_{\text{crush}} \tag{A.11}$$

where ρ is the current density, $\mu = \rho/\rho_0 - 1$ is the volumetric strain, ρ_0 is initial density. $K_{\text{elastic}} = p_{\text{crush}}/\mu_{\text{crush}}$ denotes the elastic bulk modulus. p_{crush} and μ_{crush} represent the pressure and volumetric strain that occur at crush in a uniaxial stress compression test, respectively.

(2) Transition zone

This region occurs at $p_{\text{crush}} \leq p \leq p_{\text{lock}}$, where the material is at the plastic transition state. In this region, air voids are gradually compressed out of the concrete and plastic volumetric strain is produced.

The loading EOS is given by

$$p = p_{\text{crush}} + K_{\text{tran}}(\mu - \mu_{\text{crush}}), \quad p_{\text{crush}} \leq p \leq p_{\text{lock}} \tag{A.12}$$

where $K_{\text{tran}} = (p_{\text{lock}} - p_{\text{crush}})/(\mu_{\text{plock}} - \mu_{\text{crush}})$, $\mu_{\text{plock}} = p_{\text{lock}}(1 + \mu_{\text{lock}})/K_1 + \mu_{\text{lock}}$ denotes the volumetric strain at p_{lock}. p_{lock} represents the fully dense pressure, K_1 is a material constant. $\mu_{\text{lock}} = \rho_{\text{grain}}/\rho_0 - 1$ is the locking volumetric strain, where ρ_{grain} is the grain density.

The unloading EOS is given by

$$p = p_{\text{crush}} + K_{\text{tran}}(\mu_{\max} - \mu_{\text{crush}}) + [(1 - F)K_{\text{elastic}} + FK_1](\mu - \mu_{\max}) \tag{A.13}$$

where $F = (\mu_{\max} - \mu_{\text{crush}})/(\mu_{\text{plock}} - \mu_{\text{crush}})$ is the interpolation factor, lmax is the maximum volumetric strain reached prior to unloading.

(3) Fully dense zone

In this region, the air voids are completely removed from the concrete when the pressure reaches plock so that the concrete is completely crushing.

The loading EOS is given by

$$p = K_1\bar{\mu} + K_2\bar{\mu}^2 + K_3\bar{\mu}^3 \tag{A.14}$$

where $\bar{\mu} = (\mu - \mu_{\text{lock}})/(1 + \mu_{\text{lock}})$ is the modified volumetric strain, K_1, K_2 and K_3 are constants for material with no air voids.

The unloading EOS is given by

$$p = K_1\bar{\mu}_{\max} + K_2\bar{\mu}_{\max}^2 + K_3\bar{\mu}_{\max}^3 + K_1(\mu - \mu_{\max}) \tag{A.15}$$

The tensile pressure is limited to $T(1 - D)$.

Appendix A.2.3. HJC failure criterion

An accumulated damage failure model is used in HJC model, which is written as

$$D = \sum \left[(\triangle\varepsilon_p + \triangle\mu_p) \,/\, \left(D_1 \left(p^* + T^* \right)^{D_2} \right) \right] \tag{A.16}$$

where D denotes the damage parameter, $\triangle\varepsilon_p$ and $\triangle\mu_p$ denote the equivalent plastic strain and plastic volumetric strain, respectively, during one cycle of integral computation. $T^* = T/f_c^{'}$ denotes the normalized maximum tensile hydrostatic pressure, T the maximum tensile hydrostatic pressure. D_1 and D_2 are the damage constants. In order to allow for a finite amount of plastic strain to fracture, a third damage constant E_{fmin} is provided.

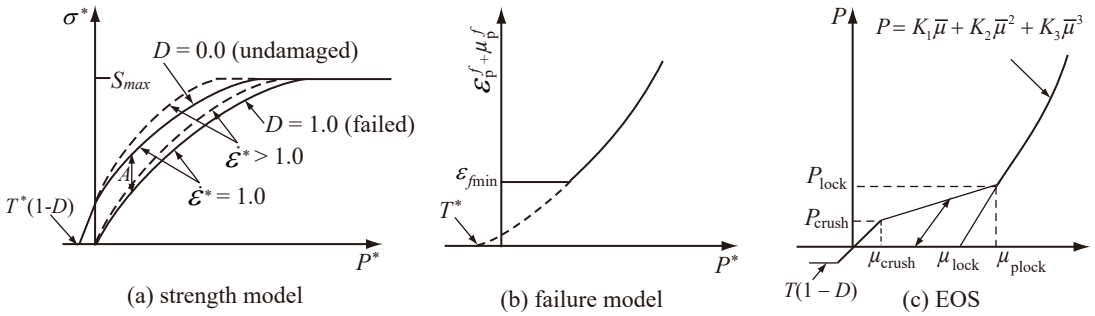

Figure A.33: HJC constitutive model of concrete

Appendix B. Description of crack

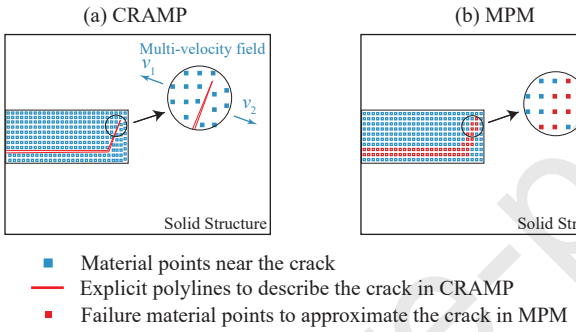

Figure B.34: Description of crack

The implementation of cracks within the framework of the MPM mainly includes two kinds of simulation methods. In the first kind, the multiple velocity fields are applied to describe the crack. Nairn proposed a method named CRAMP (MPM with cracks) which simulates a crack by three types of velocity fields: one for particles on the same side of the crack relative to the node, one for particles above the crack relative to the node, and one for particles below the crack relative to the node[70]. On the contrary, the pure MPM does not introduce the explicit crack, but uses a collection of failure particles to determine the approximate position of the crack.

The crack tip in the CRAMP is acute, while that in the pure MPM is diffused. Therefore, the disadvantage of the pure MPM is that the crack is mesh dependent. However, CRAMP needs to describe the crack with polylines, classifies both sides of the crack as two components with different velocities and apply contact algorithms. In contrast, the pure MPM classifies failure particles and other particles as two components in the same velocity field and apply the contact algorithm. Hence, the pure MPM is simple and computational efficient. Therefore, the pure MPM is employed to describe the crack in this paper. A more accurate crack description method will be realized in the future work.

Declaration of interests

☒ The authors declare that they have no known competing financial interests or personal relationships that could have appeared to influence the work reported in this paper.

☐The authors declare the following financial interests/personal relationships which may be considered as potential competing interests:

Ruichen Ni: Conceptualization, Methodology, Software, Validation, Formal analysis, Data Curation, Writing - Original Draft, Visualization

Jiasheng Li: Software, Validation, Formal analysis, Data Curation, Visualization

Xiong Zhang: Conceptualization, Methodology, Writing - Review & Editing, Supervision, Project administration, Funding acquisition

Xu Zhou: Validation, Investigation, Supervision, Project administration, Funding acquisition

Xiaoxiao Cui: Validation, Investigation, Data Curation, Supervision